Atomic Force Microscopy of Nanoparticles and Biological Cells

Inauguraldissertation

zur

Erlangung der Würde eines Doktors der Philosophie

vorgelegt der

Philosophisch-Naturwissenschaftlichen Fakultät

der Universität Basel

von

Matthias Wasem

aus Wattenwil, BE

Basel, 2015

Genehmigt von der Philosophisch-Naturwissenschaftlichen Fakultät

auf Antrag von:

Prof. Dr. Ernst Meyer
Prof. Dr. Martino Poggio

Basel, den 17.02.2015

Prof. Dr. J. Schibler, Dekan

Abstract

Nanoparticles are of great interest in science and industrial application. The high surface to volume ratio offer very distinct physical properties compared to their corresponding bulk material. One of the most powerful tools to investigate nanoparticles and generally the nano-world is the Atomic Force Microscopy (AFM). This instrument offers unique applications for the analysis of nanoparticles, from imaging to manipulation up to assignment of their intrinsic physical properties. It also enables to perform experiments in various environments from liquids to ultra-high-vacuum (UHV) and temperatures down to the low Kelvin regime. The following presented thesis is structured into three parts.

In the first part, the retention properties of calcium fluoride (CaF_2) nanoparticles on mica and human tooth substrate in liquid and at room temperature are discussed. These nanoparticles are promising candidates as additives in dental care products, which could serve as possible fluoride-container to prevent carries. I will focus on exploring the adhesion strength of as-synthesized calcium fluoride nanoparticles adsorbed on mica and on tooth enamel in liquid with Amplitude Modulation AFM (AM-AFM), depending on the substrate roughness and the chemical interplay between substrate and nanoparticles.

In the second part of the thesis pathogene *Escherichia coli* (*E. coli*) bacteria are investigated under ambient conditions. Treatment of these bacteria with the human antibody immunoglobulin A (IgA) was found to inhibit the pathogenicity of these bacteria. The aim was to explore how the IgA affects the morphology of native bacteria and to show where and how this biomolecule can be found on the cell.

The third question is then a combination between both previous questions. It combines nanoparticles and bacteria. The magnetic properties of one single magnetotactic bacteria (MTB) is investigated with AFM under UHV conditions at cryogenic temperatures. Magnetotactic bacteria have magnetosomes incorporated in their body. These magnetosomes consist of nanometer-sized iron oxide (magnetite) particles used for the bacteria to sense the earths magnetic field to find optimum living conditions. Biogenic produced iron oxide nanoparticles are interesting for various fields in science.

To conclude, the three main goal of this PhD is to answer at the following questions:

- Are CaF_2 nanoparticles suitable candidates, in respect to their adhesion properties, to be used against caries in dental care products?

- How does the immunogloublin A modify the morphology of *E. coli* bacteria so they can not cause infections anymore?
- What is the magnetic property of one single MTB of the *Magnetospirillium gryphenwaldense* bacteria species?

To answer the above questions, the AFM is used in various environments, from measuring in liquid (question 1) to ambient (question 2) to ultra low temperature UHV conditions (question 3). This thesis once more shows how powerful the AFM is, not only with respect to surface related problems but also might answer questions regarding material properties.

Contents

List of Figures

List of Tables

Chapter 1

Theoretical Background

In this chapter the theoretical background is presented. First, a short introduction to AFM the different operating modes and the relevant forces is presented. In a second part the AFM as a manipulation tool is discussed. In the last part, magnetotactic bacteria and the cantilever magnetometry method are introduced, a technique to examine the magnetic properties of such bacteria.

1.1 Atomic Force Microscopy

Different operating modes are used within the AFM set-up, which can be classified into dynamic and static modes.

1.1.1 Contact Mode AFM

In the static operating mode, also called the contact mode, a cantilever is in contact with a desired sample while scanning. The overall forces are determined by repulsive forces. Keeping the normal force F_N with a feedback-loop constant, maps of equal normal forces are obtained. The static vertical deflection signal δz of the photodiode is then proportional to the applied normal force:

$$F_N = -k_N \Delta z, \tag{1.1}$$

where k_N is the normal spring constant. Is the scan direction perpendicular to the cantilever axis, the horizontal deflection signal is then equal to the frictional forces of the contact. In this case, the lateral force acting on a tip is proportional to the torsion of the cantilever [1].

1.1.2 Amplitude Modulation AFM (AM-AFM)

There are two important imaging modes known in the dynamic mode: the frequency modulation mode (FM-AFM) and the amplitude modulation mode (AM-AFM). In the FM-AFM mode, also referred to as the non-contact mode, the tip-sample distance is controlled by modulating the frequency shift of the oscillating cantilever. The tip is held in a close proximity to the surface, enabling the detection of short range forces. Under UHV conditions even sub-molecular features have been imaged [2]. Under ambient conditions a mayor problem rises when measuring in the FM-AFM mode: the meniscus layer formed on most surfaces [3]. This layer will force the tip to snap into contact. To prevent snap to contact cantilevers with stiffness larger than $\approx$ 10 N/m (atom equivalent spring constant) are used [4]. Under UHV conditions, ultra-high resolution is obtained by means of qPlus sensors [5]. The much higher stiffness of the sensor, with spring constants of $\approx$ 1800 N/m, enables measuring at higher forces and lower amplitudes preventing snap to contact.

For dynamic mode AFM measurements performed under ambient conditions, the AM-AFM mode is the most used. In this mode the cantilever is excited close to its free resonance frequency, where the tip-sample distance is controlled via modulation of the amplitude. As the cantilever is touching the sample surface at the bottom of each oscillation cycle, this mode is also called tapping mode. In tapping mode AFM the equation of motion of a cantilever-tip can be simulated as driven by a sinusoidal external driving signal and a damping term [6–8]. The movement of the cantilever is then described as follows:

$$m\ddot{z} = -k_c z - \frac{m\omega_0}{Q}\dot{z} + F_{ts} + F_0 cos(\omega t), \tag{1.2}$$

where k_c is the spring constant, z the displacement of the cantilever, ω_0 the angular resonance frequency, Q the quality factor of the free cantilever, F_{ts} the tip-sample interaction force, F_0 the excitation force of the actuator and ω the angular excitation frequency. The cantilever motion described within this equation is governed by four parts: the elastic response of the cantilever, the overall hydrodynamic damping of the system, the tip-sample interaction forces and the sinusoidal driving force. The tip sample interaction force F_{ts} includes long-range attractive van der Waals forces (vdW), short range repulsive forces and contact forces. For the short-range and contact forces, different contact models like the Johnson-Kendall-Roberts (JKR) [9] or the Derjaguin-Muller-Toporov (DMT) [10] models are applied to give an analytical relationship between applied force and deformation. Compared to contact mode AFM the destructive lateral forces are virtually eliminated in AM-AFM as the probing tip has a much lower contact time

while mapping the surface, resulting in a much more gentle sensing of the investigated surface [11, 12]. AM-AFM has the ability to measure simultaneously the surface morphology and the compositional variations of the mapped surface. These variations are detected by recording the phase-lag of the excitation signal with respect to the vibrating tip, known as the phase imaging technique. The phase images so-generated are closely related to energy dissipation maps [13, 14]. While phase imaging under ambient conditions with high quality cantilever factors is well established [15], a comprehensive model of the energy dissipation process since the first studies of AM-AFM measurements in liquid [16, 17] is still missing. Recent experiments in liquid have related the phase contrast (where low Q-factors are found), to have two origins: the excitation of higher eigenmodes and the energy dissipation on the sample surface [18, 19].

1.1.3 Force Modulation Microscopy (FMM)

Force modulation microscopy (FMM) or simply tapping in contact, stands for an operating mode where a contact cantilever is used to scan the surface in the contact mode in which additionally the cantilever is excited at the contact resonance [20]. This oscillation causes a modulation of the static interaction force between tip and sample. The damping of the oscillation amplitude depends on the stiffness of the contact [21]. Is in the FMM mode the contact resonance frequency controlled with a PLL (Phase-lock-loop), from the frequency shift of the contact resonance it is possible to determine the contact stiffness and calculate the E-modulus of the substrate [22]. Figure 1.1 shows a sketch of how the phase and amplitude response of the cantilever in FMM mode is sensitive to the stiffness of the contact.

1.2 Relevant Forces

In this section the relevant forces acting while imaging with AFM will be discussed. These forces are also relevant in understanding particle adhesion phenomena.

1.2.1 van der Waals Forces

Van der Waals forces are defined as non-covalent forces which rise from non-permanent dipole-dipole interactions between atoms or molecules. Fluctuations of dipole moments cause a temporary polarization as a result of random fluctuation of the electron density or due to the interaction of dipoles induced by the electric field of a neighbouring atom. These forces are always present even in chemically inert noble atoms. Van der Waals forces are

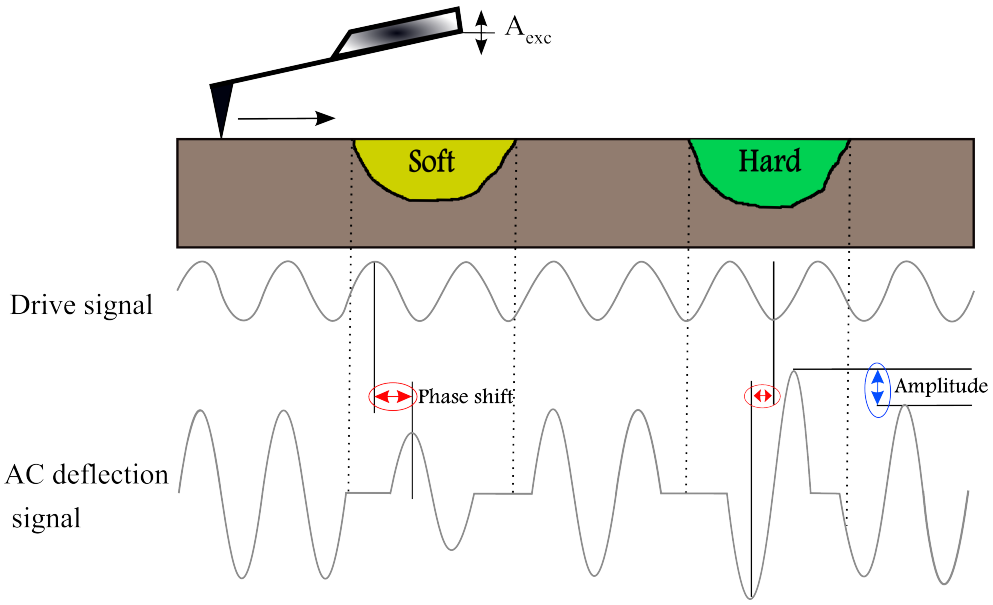

Figure 1.1: Illustration of how amplitude and phase variations of the cantilever depend on the mechanical properties of the substrate in the FMM mode. The Z feedback loop maintains a constant cantilever deflection (constant normal force) whereas the cantilever is simultaneously excited at the contact resonance frequency with an excitation amplitude A_{exc}. Local variations of the sample stiffness, result in reduction (soft material) or increase (hard material) of the amplitude response of the oscillation. Similarly, the phase shift is changed on the different material sites.

very weak, but by summing them up they can be very strong. For example geckos use them to climb up on nearly any surface only due to the high number of tiny hairs, which can adapt even to rough surfaces and where every single one is attracted to the surface via van der Waals forces. Van der Waals forces are very distance dependent, at short distances the force F_{vdW} is proportional to $1/r^7$ but at a distance $r \approx 5$ nm the power law reduces to $1/r^8$. If one assumes the cantilever tip to be a sphere approaching a semi-infinite flat surface, the vdW force is given by:

$$F_{vdW} = HR/6D^2, \tag{1.3}$$

where H denotes the Hamaker-constant which depends on materials and the medium between them, R is the radius of the tip and D is the tip-sample distance.

1.2.2 Electrostatic Force

Forces acting on a tip can also rise from the interaction between localized electrical charges. These charges can be deposited either by contact electrification (CE) or by corona discharge (CD) [23]. The distance dependent strength of the electrostatic force obeys the law of Coulomb. The electrical force acting between a conducting tip and a localized charge can be described by:

$$F_{charge} = q_i E_z, \tag{1.4}$$

where q_i denotes the charge on the tip and E_z the electric field. Another contribution to the total electrostatic force is given by the capacitive force. One can describe the tip-sample situation as a capacitor, where the force is described by means of a distance dependent capacitance C. This force is then given by:

$$F_{capacitance} = \frac{1}{2}\frac{\partial C}{\partial z}(V_{bias} - V_{cpd})^2, \tag{1.5}$$

where V_{bias} is the applied voltage and V_{cpd} the contact potential difference between tip and sample. The capacitance strongly depends on the geometry of the tip and if we assume the tip to be a sphere which is very far away from the surface, we can write [24]:

$$F_{capacitance} = \pi\epsilon_0 \left(\frac{R}{z}\right)^2 (V_{bias} - V_{cpd})^2, \tag{1.6}$$

where R is the tip radius, z the tip-sample distance and ϵ_0 the dielectric permittivity. The total electrical force is the sum of static and dynamic contributions coming from F_{charge} and $F_{capacitance}$ [4].

1.2.3 Adhesion Mechanisms of Particles Adsorbed on Surfaces

Particle adhesion classifies a situation where the predominant forces rise from forces present in the particle-substrate interface. These forces can be separated into short-range forces and long-range forces The long-range forces, like van der Waals and electrostatic forces, can be regarded as the forces that bring the particle into contact with the surface. As soon as the particle-substrate contact is done, the short-range forces start to act. How nanoparticles are adsorbed and adhere on surfaces is still not fully understood. Adhesion mechanisms might be classified into a theory of particle adhesion and liquid-mediated adhesion [25]. The liquid-mediated adhesion occurs due to ther surface energy of the liquid. This is for instance the

adhesion mechanism for pressure-sensitive adhesives [26]. Pressure sensitive adhesion can also be regarded as an example of a physical adsorption mechanism. For long timescales (wetting) it behaves as a liquid and for short timescales (peeling) as a solid [27]. In the broadest sense one can understand adhesion to be a result of physical- and chemical interaction forces. Physical adhesion is mostly due to van der Waals attraction forces and acid-base interactions, like hydrogen bonds [28]. Chemical adhesion involves covalent bonding, ionic or electrostatic bonds, coordinate bonds and metallic bonds [29]. The chemical adhesion is much stronger than the physical adhesion. In comparison to van der Waals forces, covalent bonding happens through direct electron exchange between the adhered materials and is therefore much stronger. Adhesion of particles can also arise from mechanical interlocking of macromolecules [30] or mechanical interlocking through particle and substrate shape effects, like pores, holes or scratches, determined by the surface roughness [31]. The electrostatic adhesion, rising as a result of electrostatic bonding, is another important adhesion mechanism [32, 33]. For example in laser printers and photocopiers this is an important force behind their functionality (also called xerography). The adhesion properties of polymers, which are of high interest for the industry, also show a high diversity of adhesive phenomena. Van der Waals attraction and chemical bonding but also other factors are known to be involved in polymer adhesion. It is known to occur inter-diffusion of polymeric chains at the interface, which greatly enhance the adhesion strength [34] or charge separation where an electrostatic component has to be taken to account [35]. The forces contributing to the overall adhesion force between interfaces is a very diverse and broad field in surface science.

1.3 AFM as Manipulating Tool

Since the historical manipulation experiment of a single atom performed with Scanning Tunneling Microscopy (STM) under UHV conditions by Eigler *et al.* [36] numerous methods have been developed and used to precisely manipulate nanostructures with Scanning Probe Microscopy (SPM) techniques. Despite the very high level of accuracy to perform controlled manipulation experiments with STM, it fails to determine the dissipated energy involved in the manipulation process. AFM offers the possibility to measure the energy needed for manipulation. Although the total dissipated energy is measured, it is very difficult to separate which amount of energy is dissipated from the particle-substrate-, tip-sample- or tip-particle interaction. Another advantage of AFM as a manipulating tool is that manipulation measurements can be performed on non-conducting surfaces and in liquids.

First, manipulation studies of AFM in contact mode and tapping mode are presented. Further the focus will be on the theory of AM-AFM manipulation and how the dissipated energy can be measured with this technique.

1.3.1 Manipulation in Contact Mode

Manipulation experiments of nano-sized objects are routinely done using the AFM in the contact mode [37, 38]. The interfacial friction forces between the substrate and particle were already investigated depending on the morphology of the particles and orientation of the manipulation pathway [39] and the environment [40]. Dietzel *et al.* [41] also used two distinct strategies to manipulate nanoparticles in the contact mode with an AFM tip: in the first case the tip was used to push the particles and in the second case the tip was put on top of the particles to perform manipulation. Large islands of C60 molecules have also been manipulated successfully on NaCl in the contact mode under UHV conditions [42].

1.3.2 Manipulation in the AM-AFM Mode

Some studies have been reported performing controlled manipulation of nanoparticles in tapping mode AFM. Sitti *et al.* [43] used a cantilever probe in the dynamic mode to manipulate as-synthesized latex nanoparticles on Si under ambient conditions . Other authors manipulated antimony nanoparticles [44] and gold nanoparticles [45] on graphite also under ambient conditions. Mougin and co-workers moved as-synthesized and functionalized gold nanoparticles on silicon substrates with dynamic AFM [46]. Darwich *et al.* [47] investigated the retention of gold colloidal nanoparticles with tapping mode AFM depending on the particle-substrate affinity and humidity. In all these manipulation studies the major difficulty arises from the quantification of the involved dynamic processes, i.e. the collision between the probing tip and the particle, the friction and the electrostatics between the particles and the substrate and the role of water when measuring in ambient (lubrication, capillary effects, etc.).

1.3.3 Theory of Particle Manipulation and Probe Trajectory in AM-AFM

The following section will explain briefly the theoretical background for manipulation experiments performed with AM-AFM. The theory is derived from a work written by Rao *et al.* [48]. For simplicity, the theory was deduced for spherical particles where only sliding without rolling was assumed. The theory is also valid for other particle shapes when no rolling or canting of the particles is observed during the manipulation process. The theory is

very similar to the classical elastic scatter theory, where upon collision the kinetic energy of a particle is conserved in the center-of-mass frame. The deflection direction of particles strongly depends on the scan path of the AFM tip. We will just discuss the situation when the tip is scanning the surface in the raster scan path. In this case, the particles are deflected in a direction defined by the geometries of the probing tip, the particle-sample contact area and the spacing between the consecutive scan lines of the AFM probe in the slow scan direction. In figure 1.2 a schematic top view of a tip colliding with a spherical particle is illustrated. In this case the radius of the particle is big compared to the tip radius. R_1 and R_2 correspond to the radius of the tip and the particle, respectively. In a two dimensional situation, α is the collision angle between the center of mass of the tip and the particle. In reality, the tip and the particles have a 3D shape and one has to take into account the aperture angle of the tip to describe the particles-substrate radius. With except for the first scan line, the displacement angle of a particle θ with respect to the fast scan axis can be written as:

$$\tan\theta = -\frac{b}{R(\cos\alpha_0 + \log\tan\frac{\alpha_0}{2})}, \tag{1.7}$$

where R defines the intrinsic particle-substrate contact radius, b the spacing between consecutive scan lines in the slow scan direction and $\alpha_0 = \arcsin\left(1 - \frac{b}{R}\right)$. The collision angle α_0 depends on the initial position of the particle and is always the same, except for the first scan line.

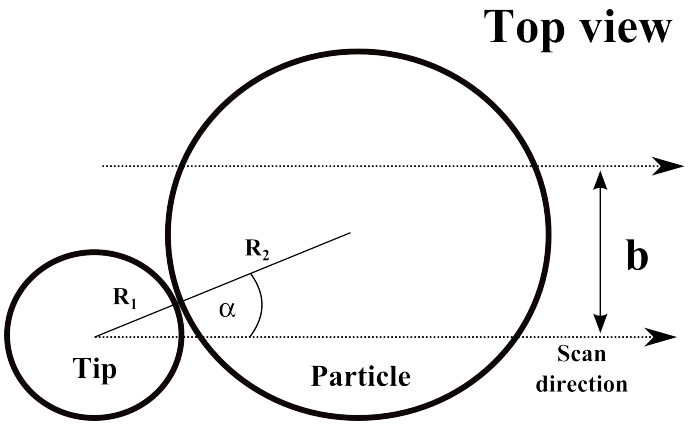

Figure 1.2: Schematic 2D view of a tip colliding with a spherical particle, for the situation where $R_1 < R_2$. b represents the spacing between consecutive scan lines in the slow scan direction and α the angle of collision between both center of masses.

The theoretical predicted deflection angle θ, for a tip radius of $R_1 = 10$ nm, an aperture angle of 10° and a spacing between consecutive scan lines $b = 39$ nm calculated with Eq. (1.7) is illustrated in figure 1.3. A deflection

angle approaching 90° is reached for large particle-substrate contact radii. In case of particles with a plane facing adsorbed on a smooth and atomically flat substrate, where always the same cantilever tip radii and the same b values are assumed, the distribution of the trajectory angle can be regarded as the size distribution of the synthesized particles.

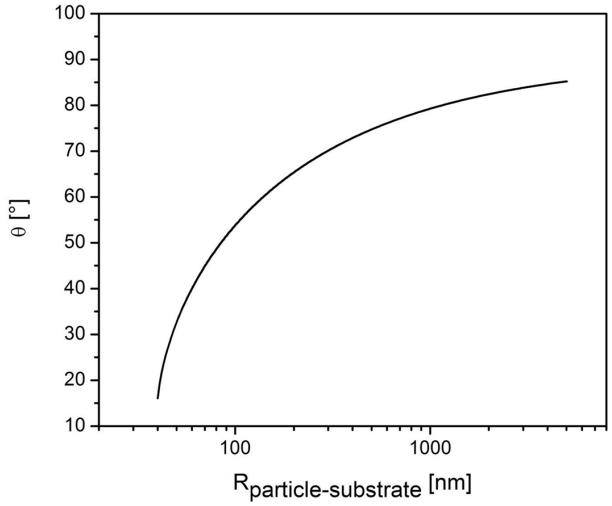

Figure 1.3: Theoretically predicted trajectory angles θ of nanoparticles manipulated in the AM-AFM mode. A cantilever tip radius of $R_1 = 10$ nm, an aperture angle of the tip of 10° and a spacing between consecutive scan lines in the slow scan direction of $b = 39$ nm was assumed for calculation. Using similar cantilevers with comparable tip radii, the deflection angle θ saturates to 90° for very big particle-substrate radii.

1.3.4 Power Dissipation in AM-AFM

Manipulation experiments in AM-AFM are difficult to quantify as dynamical- and frictional processes are involved at the same time. However, to gain information about the work that is needed to change the position of nano- or microsized object, one can measure the damping of the oscillating cantilever. The damping of the cantilever is then related to the energy that is transferred form the tip to the displaced object. The derivation of AM-AFM energy dissipation is described by Cleveland *et al.* [13]. If we assume a system in equilibrium, the average input energy must equal the average output dissipated energy. In terms of AM-AFM the average power to drive the cantilever oscillation by an external source must equal the average power that is dissipated by the cantilever and the tip. In this dynamic steady-state equilibrium one can describe the total dissipated power by the body of the cantilever as $\overline{P_{in}} = \overline{P_0} + \overline{P_{tip}}$. Where $\overline{P_{in}}$ denotes the input power to drive the oscillation. $\overline{P_0}$ can be regarded as the average power dissipated by the body

of the cantilever (i.e. air damping or damping of the cantilever motion in the liquid) and can be modeled by simple viscous damping. The second part $\overline{P_{tip}}$, corresponds to the power dissipated by tip-sample interactions. The input power $\overline{P_{in}}$ can be calculated for a cantilever with a spring constant k whose base position $z_d(t)$ is excited sinusoidally with a drive amplitude A_d and a frequency ω. In AM-AFM the steady-state response of the cantilever can be assumed as sinusoidal, the deflection from equilibrium of the end of the cantilever $z(t)$ can be written as $A\cos(\omega t+\phi)$, where A is the amplitude of the cantilever and ϕ the phase response of the cantilever relative to the actuator. The instantaneous power delivered by the actuator is then the force from the actuator F times the velocity of the actuator $\dot{z_d}$:

$$P_{in} = F\dot{z_d} = k\left[z(t) - z_d\right]\dot{z_d}. \tag{1.8}$$

If we integrate this over a whole oscillation cycle, the average power dissipated by the actuator yields to:

$$\overline{P_{in}} = \frac{1}{2}kA_dA\omega\sin(\varphi). \tag{1.9}$$

This expression shows that the maximum power delivered to an oscillator happens when the phase response is $\varphi = 90°$ with respect to the actuator. Now we will address the power that is leaving the cantilever. Assuming a background dissipation P_0 which can be modeled by viscous damping of the cantilever body, $F_{damping} = \eta\dot{z}$, a similar analysis as performed above yields to an average background power:

$$\overline{P_0} = \frac{1}{2}\eta A^2\omega^2. \tag{1.10}$$

The power dissipated by the tip can now be solved, as one can easily experimentally measure η, through Q_{cant}=$k/b\omega_0$, where Q_{cant} is the quality factor and ω_0 the natural resonance frequency of the cantilever:

$$\overline{P_{tip}} = \frac{1}{2}\frac{kA^2\omega_0}{Q_{cant}}\left[\frac{Q_{cant}A_d\sin(\varphi)}{A} - \frac{\omega}{\omega_0}\right]. \tag{1.11}$$

In this equation, Q_{cant} and ω_0 express the viscous damping coefficient η, described in equation (1.10), in terms of experimentally accessible quantities. According to equation (1.11) the power lost by tip-sample interaction is proportional to the sine of the phase-lag. It is important to note that this equation allows the calculation of the total energy lost by tip-sample interactions but does not reveal how exactly it is lost. It also assumes that the pristine quality factor Q_{cant} of the oscillating cantilever does not change during a measurement (no tip change, no change of cantilever clamping and no change of viscous damping, etc.). As the drive frequency is mostly chosen

to be ω_0, Eq. (1.11) can be simplified, when we define the free amplitude of the cantilever as A_0=$Q_{cant}A_d$, resulting in:

$$\overline{P_{tip}} = \frac{1}{2}\frac{kA^2\omega_0}{Q_{cant}}\left[\left(\frac{A_0}{A}\right)\sin(\varphi) - 1\right]. \tag{1.12}$$

The most important consequence from this equation is that if the tip does not loose energy, the amplitude and the phase are not independent. This means that when imaging is done with the amplitude held constant by the feedback loop, which is the case in AM-AFM, phase contrast is only observed when energy is lost through tip-sample interaction. There is one exception in which phase contrast is also observed but is not coming from power being dissipated. From Eq. (1.12) one can see that the phase-lag is proportional to $\sin(\varphi)$ rather φ itself. Since the sine is a symmetric function around 90°, symmetric phase changes around 90° are allowed even if no energy is lost from tip-sample interaction. Such discontinuous jumps around 90° were shown to arise from competition between attractive and repulsive forces under certain experimental conditions [49]. Phase jumps ($> 90°$) are attributed to attractive and ($< 90°$) to repulsive interaction forces. More about this phenomena typical in AM-AFM is discussed in the next section about amplitude bistability. As long as the phase stays at one side of 90° (attractive or repulsive regime), the phase changes (or phase images) can directly be attributed to the power being lost through changes in the interaction between the probing tip and the sample.

1.3.5 Amplitude Bistability in AM-AFM

Amplitude bistability in AM-AFM is a consequence of the coexistence of two oscillating states of the tip, oscillating near a surface or in intermittent contact with a surface [50]. It is a result of the non-linear force gradient (long range attractive- and short range repulsive forces) at different tip-sample separations. This non-linear force gradient modifies the compliance of the cantilever and hence induces a change in the oscillation amplitude due to a shift in the tip resonance [51]. The numerical solution of Eq. (1.2) for a range of free amplitudes and specific E-moduli in the DMT contact deformation model, showed that the oscillation has mathematically two different solutions, a low and high amplitude solution [52]. The low and high amplitude solutions correspond to a situation where the tip is sensing either a net attractive tip-sample force gradient or a net repulsive tip-sample force gradient. The phase-shift between the oscillation and the actuator to maintain the oscillation, can be used to distinguish between both operating regimes. In the previous section it was shown that the maximum power delivered from an actuator to a harmonic oscillator occurs when the

response is 90° out of phase with the actuator. In figure 1.4 the experimentally measured phase response is shown for a cantilever oscillating at a free amplitude of $A_0 = 7$ nm where amplitude bistability occurs, depending on the tip-sample separation. In the regime Z = [0:6], the cantilever oscillation is not influenced by attractive tip-sample interaction forces and their gradient, the phase shift equals 90°. This does not imply that there are no forces present, the cantilever is just not sensitive enough to sense them. Decreasing the tip-sample distance results in an increase of the phase up to a point where the phase changes from values above to below 90°. This regime marks the transition from the tip oscillating in non-contact to intermittent contact with the surface (i.e. a change in the force gradient from a net attractive to a net repulsive tip-sample force situation). Whether the tip is in the attractive or repulsive region has been described to depend on factors such as the free amplitude, the sample mechanical properties (interaction surface potential), the tip radius and the cantilever spring constant [53]. It has also been reported that for soft samples, like biomolecules, bistabilities occur more frequently [49]. The occurrence of amplitude bistability strongly being influenced by the intrinsic sample mechanical and adhesive properties will be discussed in more detail in the chapter about the imaging of *E. coli* bacteria.

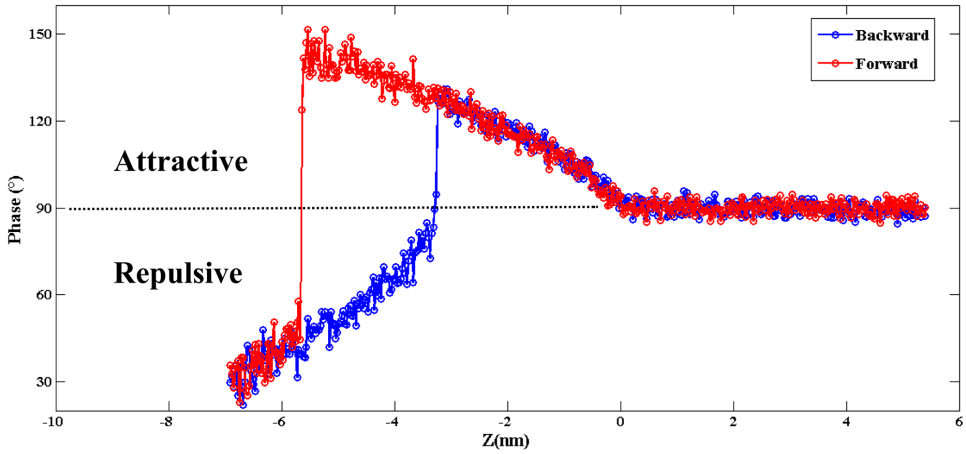

Figure 1.4: Experimentally measured phase response depending on the tip-sample distance taken over a bacterium. The cantilever oscillation frequency was $f = f_0 = 183.2$ kHz and the free amplitude $A_0 = 7$ nm. At Z = 0 the cantilever tip starts to interact with the sample due to sensing of attractive long-range interaction forces. The discontinuous jump in the phase is due to the transition from the tip oscillation in non-contact to intermittent contact with the surface.

1.4 Cantilever Magnetometry

Several techniques exist to examine the magnetic properties of micro- to nano-sized materials. Micromechanical cantilevers used in AFM are highly sensitive to small forces and very suitable to be used as sensors for exploring the magnetic properties of materials or particles. In traditional Magnetic Force Microscopy (MFM), sensing of the magnetic force happens by detecting the stray fields above the magnetic material [54, 55]. Contrary, in Dynamic Cantilever Magnetometry (DCM) the magnetic properties of the entire magnetic volume is examined, as the material itself is placed at the free end of an oscillating cantilever. In this work we used Dynamic Cantilever Magnetometry to determine the magnetic properties of a single magnetotactic bacterium. This set-up enables to measure the magnetization, demagnetization and the magnetization reversal mechanisms of the material within a short response time of a few cantilever oscillations. In DCM, the torque τ acting on a cantilever in an external magnetic field $\vec{H}_{ext}$ depends on the magnetization $\vec{M}$ which in return is specific to the magnetic properties of the attached magnet:

$$\tau = \mu_0 V(\vec{M} \times \vec{H}_{ext}), \tag{1.13}$$

where μ_0 is the magnetic permeability in vacuum and V the magnetic volume of the particle. A shift of the eigenfrequency due to this torque is then recorded depending on the external applied magnetic field. Since the torque depends on the perpendicular component of magnetization to the magnetic field, it is sensitive to any kind of magnetic anisotropy like shape or crystalline magnetic anisotropy [56]. The contribution of the magnetization to the shift the eigenfrequency of the cantilever can be thought as an additional spring constant which is caused by the interaction of the magnetic particle with the external magnetic field. From the frequency shift response of the cantilever as a function of the applied external magnetic field, so called f-H curves, the magnetic properties of the sample can be derived. By fitting the obtained f-H curves with an adequate model, the intrinsic magnetic properties, like the magnetic moment or the anisotropy constant of the attached magnetic material can be derived. In the next section we will derive the model which was used to fit the experimental measured DCM f-H curve from a single magnetotactic bacterium.

1.4.1 Cantilever Magnetometry of Ferromagnetic Particles

Compared to paramagnetic materials, where the magnetization uniquely depends on the external applied magnetic field, the case is different for

ferromagnetic materials. Ferromagnetic materials show a magnetic field dependent hysteresis. Magnetic hysteresis is an effect caused by a change of the magnetic domain ensemble, where the orientation and the magnetization of each single magnetic domain changes relative to the external magnetic field. First, we will derive the model for a spherical ferromagnetic particle with an uniaxial demagnetization. In this case we can use the Stoner and Wohlfarth model for the magnetization of a single domain ferromagnet [57]. In this model the magnetization $\vec{M}$ does not vary within the particle as it is uniaxial and the external magnetic field $\vec{H}_{ext}$ just varies along one single axis. The magnetization vector then rotates along one angle as the magnetic field changes. Figure 1.5 shows the geometrical and relevant parameters needed to derive the model.

From thermodynamic considerations the free energy of a closed system is minimized at thermal equilibrium. To find the magnetization equilibrium for a spherical ferromagnetic single domain particle with an uniaxial demagnetization in a magnetic field, we have to find an angle ϕ_{min} between the magnetization of the particle $\vec{M}$ and the externally applied magnetic field $\vec{H}_{ext}$, where the total free energy of the system is minimized [58]:

$$\tilde{F} = \int (\tilde{F}_0 - \frac{1}{2}\mu_0 \vec{M}(\vec{H}_{int} + \vec{H}_{ext}))dV. \tag{1.14}$$

In this equation, $\tilde{F}_0$ describes all kind of anisotropies except shape anisotropy $\vec{H}_{int}$ the internal magnetic field vector of the particle and V the volume of the magnetic particle. The free energy of a magnetic particle in a magnetic field described with this equation is a combination of the potential energy of the particle interacting with the external field and the intrinsic demagnetization factors of the particle. The magnetic anisotropy $\tilde{F}_0$ for uniaxial anisotropy can be written as:

$$\tilde{F}_0 = KV sin^2(\beta - \phi), \tag{1.15}$$

where β is the cantilever oscillation around the y-axis, K the anisotropy constant and ϕ the angle between the magnetization and the magnetic field. For a spheroid where the polar axis is fixed, Stoner and Wohlfarth [57] attested that the equilibrium magnetization lies in the plane spanned by the external magnetic field and the spheroid's polar axis. The magnetization vector $\vec{M}(\phi)$ as a function of the angle ϕ can then be written as:

$$\vec{M}(\phi) = (0, M\cos(\phi), M\sin(\phi)). \tag{1.16}$$

The internal magnetic field $\vec{H}_{int}$ of a particle in the laboratory system

can be described as follows:

$$\vec{H}_{int} = \vec{H}_{ext} - \hat{N}\vec{M}(\phi), \tag{1.17}$$

where $\hat{N}$ is the demagnetization tensor. This expression describes the magnetic field inside a body as a combination of the external magnetic field and the intrinsic demagnetization factors of the particle. The demagnetization tensor in the cantilever system $\hat{N}_{osc}$ only depends on the geometry of the particle and is composed from the diagonal elements N_x, N_y and N_z:

$$\hat{N}_{osc} = \begin{pmatrix} N_x & 0 & 0 \\ 0 & N_y & 0 \\ 0 & 0 & N_z \end{pmatrix}. \tag{1.18}$$

The sum over all diagonal elements is always equal to 1. For the case of a spherical particle where the demagnetization is the same at all points within a given body, the diagonal elements have all the same value of $\frac{1}{3}$. We then have to transform the demagnetization tensor from the cantilever system into the laboratory system with the rotation matrix $\hat{S}$ and the deflection angle β of the cantilever due to the oscillation:

$$\hat{S} = \begin{pmatrix} 1 & 0 & 0 \\ 0 & \cos(\beta) & -\sin(\beta) \\ 0 & \sin(\beta) & \cos(\beta) \end{pmatrix}. \tag{1.19}$$

The demagnetization tensor in laboratory system $\hat{N}$ can then be written:

$$\hat{N} = \hat{S}\hat{N}_{osc}\hat{S}^{-1}. \tag{1.20}$$

As now all parameters are derived to describe the free energy of the system, we have to differentiate the free energy with respect to the angle ϕ. If we expand into Taylor series for small cantilever oscillation amplitudes z and small angles ϕ and set this to zero, we are able to find the angle ϕ_{min} where the free energy $\tilde{F}$ is minimized. The torque $\vec{\tau}$ acting on the particle at magnetization equilibrium can then be written as:

$$\vec{\tau} = \mu_0 V(\vec{M}(\phi_{min}) \times \vec{H}_{ext}). \tag{1.21}$$

Assuming the torque to be equivalent to the force F acting on the magnetic particle, we can write the force as:

$$F = |\vec{\tau}| / \tilde{L}, \tag{1.22}$$

where $\tilde{L}$ is the reduced length of the cantilever and is calculated from $\tilde{L} = L/\alpha$, where L is the total length of the cantilever and $\alpha = 1.377$ for the first eigenmode [59]. The frequency shift resulting from the interaction of

the magnetic particle with the external magnetic field, can then be written as:

$$\Delta f = \frac{f_0}{2 \cdot k_0} \cdot \frac{\partial F}{\partial z}, \tag{1.23}$$

where f_0 and k_0 are the cantilever eigenfrequency and the spring constant in zero magnetic field, respectively. The term $\partial F/\partial z$ can be regarded as an additional spring constant, contributing to the frequency shift, as a result of the magnetic particle interacting with the magnetic field. If we expand the force into Taylor series for small cantilever oscillation amplitudes, we finally get the frequency shift response of a ferromagnetic particle:

$$\Delta f = \frac{1}{2} \frac{f_0 \mu_0 H_{ext} V M}{k_0 \tilde{L}^2} \cdot \frac{\mu_0 M^2 (N_z - N_y) + 2K}{\mu_0 M H_{ext} + \mu_0 M^2 (N_z - N_y) + 2K}. \tag{1.24}$$

There first term of the equation describes the contribution of the Zeeman energy on the frequency shift, where the second part describes the effect of the magnetic anisotropy on the frequency shift. As we want to apply the model to a cantilever magnetometry experiment of one single magnetotactic bacterium, where the magnetosome chain is best described as a rod, we just have to adjust the demagnetization tensor to one of a rod $\hat{N}_{Rod}$. The demagnetization tensor of a rod is defined as:

$$\hat{N}_{Rod} = \begin{pmatrix} \frac{1}{2} & 0 & 0 \\ 0 & 0 & 0 \\ 0 & 0 & \frac{1}{2} \end{pmatrix}. \tag{1.25}$$

Now, we can write down the equation used to fit the experimentally recorded f-H curve for one single magnetosome chain:

$$\Delta f = \frac{1}{2} \frac{f_0 H_{ext} M}{k_0 \tilde{L}^2} \cdot \frac{4KV^2 + \mu_0 M H_{ext}^2}{2MH_{ext}V + \mu_0 M H_{ext}^2 + 4KV^2}. \tag{1.26}$$

1.4.2 Limit of detection

Mainly the dimensions of the cantilever and the frequency noise determine the limit of detection of dynamic cantilever magnetometry measurements [60, 61]. The magnetic moments of a magnetosome chain of a MTB is expected to be in the range of around 7×10^{-16} Am^2 (7×10^{-13} emu) [62]. For detecting magnetic moments, smaller as 10^{-13} emu, one has to carefully choose the proper cantilever dimensions and experimental conditions. For rectangular cantilevers, the quotient described below has to be optimized to get a maximum frequency response. A reduction of the thickness basically

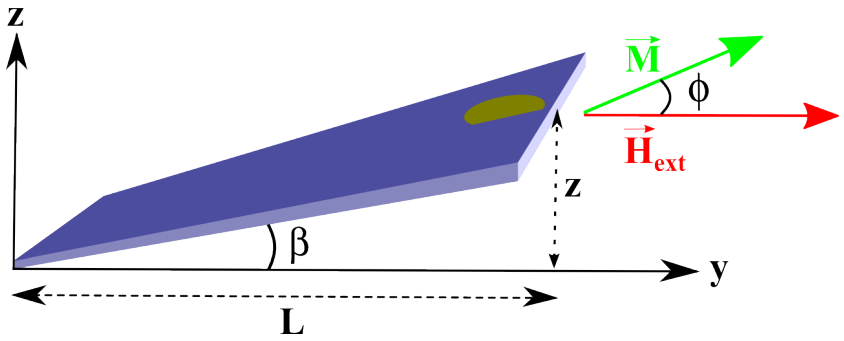

Figure 1.5: Illustration of a particle attached at the free end of a cantilever for the set up of the magnetometry experiments performed in this work. The external magnetic field $\vec{H}_{ext}$ is applied parallel to the cantilever long axis, where $\vec{M}$ is the resulting magnetization of the particle and ϕ the angle between both. L is the absolute length of the cantilever, z the cantilever amplitude and β the angle of displacement upon oscillation of the cantilever.

increase the sensitivity of the measurements:

$$f_0/(k_0\tilde{L}) \propto (Lwt^2)^{-1}, \tag{1.27}$$

where f_0 is the free resonance, k_0 is the spring constant, $\tilde{L}$ the reduced length and L the effective length and w is the thickness of the cantilever. On the other hand, the sensitivity is also limited by thermal frequency noise which is described in more detail elsewhere [63, 64]:

$$\delta f = \sqrt{f_0 k_b T B/(\pi k_0 Q A_0^2)}, \tag{1.28}$$

where k_B is the Boltzmann constant, T the temperature, B the measurements bandwidth and A_0 the oscillation amplitude. Performing measurement at low temperatures will greatly minimize thermal frequency noise.

Chapter 2

Experimental

2.1 Nanoparticle Manipulation in Liquid

Calcium fluoride nanoparticles are traditionally known to be an ideal optical material [65] and have also been tested in greases, where they showed excellent anti-wear and friction properties [66]. These particles show a wide range of use from industrial to medical purposes in bone or teeth reconstruction. In this context calcium fluoride is of high interest in saliva chemistry in reducing acid dissolution of teeth, called caries [67]. The use of CaF_2 nanoparticles as a source of fluoride for caries prevention was already discussed in earlier studies [67–69]. Dental caries is one of the most common disease of the entire world, affecting most humans. Caries is a result of the dissolution of the outermost layer of the tooth, the enamel. The enamel has the purpose to protect the inner sensitive part of the teeth against any external attack from the environment and to ensure the longevity of the dentition during a human lifetime. The solubility of this enamel layer is known to be highly pH sensitive [70]. Consumption of acidic beverages for example, directly lower the pH in the vicinity of teeth, where indirectly also bacteria in the dental plaque metabolize any source of sugars lowering also the pH on the tooth surface. If the pH drops below a certain threshold value, the tooth enamel starts to dissolve. This demineralization process of the enamel also called enamel erosion is what causes the caries disease. Little research has been done with AFM exploring tooth enamel. Studies investigated the erosion of enamel with AFM based nanoindentation and related the demineralization and remineralization processes to softening of the enamel [71, 72]. Another study performed force-distance curves with AFM tips on etched superficial enamel substrate to examine this enamel softening [73]. Incorporation of fluoride on tooth enamel has been shown to restore the hardening of the enamel layer [74, 75]. Hardening in return makes the enamel to be less affected against caries. This is why all dental

care products contain fluorated compounds. The formation of fluoride-containing nanostructures has also been observed with AFM in liquid on tooth enamel upon exposure to a fluorated solution [76]. The solubility of CaF_2 nanoparticles and hence the fluoride release is also strongly pH dependent [77]. Calcium fluoride nanoparticles are therefore possible candidates to be incorporated in dental care products as a source of fluoride. The anti-caries activity of calcium fluoride nanoparticles is mainly determined by two factors: the solubility of the nanocomposites at a certain pH and their adhesion strength to the tooth enamel upon application. One goal of this thesis is to give insight into the adhesion strength of calcium fluoride nanoparticles on tooth enamel. For this purpose, we will examine the retention properties of three CaF_2 nanoparticles which are different in respect to their size and morphology in liquid on mica and on human tooth enamel as substrate.

In a first part, we will show how the calcium fluoride nanoparticles were synthesized and discuss their structure and size. In the second part the mica and the tooth enamel samples on which the manipulation experiments were performed will be discussed. The difference between them are explained in respect to their surface texture and chemical composition. In the last part the experimental conditions are presented.

2.1.1 Synthesis of Calcium Fluoride Nanoparticles

Calcium fluoride nanoparticles were synthesized with a procedure called the precipitation method [78]. In this method, particles are formed due to an oversaturation of the solution in respect to the salt solutions, resulting in precipitation of nanosized nanoparticle. CaF_2 nanoparticles with defined morphology were prepared by mixing specific amounts of $CaCl_2$ and NaF salt solutions. The shape and size of particles synthesized with the precipitation method strongly depends on the temperature (i.e the diffusion rate) and the relative concentration of the two mixing salt solutions [79]. The size distribution of the particles on the other hand, depends on the following parameters: the degree of supersaturation in the solution, the spatial concentration distribution and the growth time of the crystals [80]. As one can not precisely control these factors, a certain size distribution of the synthesized particles is common. The precipitation method is the simplest method to produce CaF_2 nanoparticles. This method also mimics how they are formed in reality in the mouth when using fluorinated dental care products. In this case, the saliva delivers the calcium and the high amount of fluoride coming from the dental care products oversaturates the saliva with fluoride which precipitates as solidified CaF_2. The formation process of these particles in the laboratory with this method is very fast, as the solution became rapidly opaque after mixing the two solutions to-

gether. The formed nanoparticles were further purified by centrifugation and washed several times with a saturated solution of calcium fluoride to remove excess salt ions. Subsequently, the nanoparticles were vacuum dried resulting in a white powder which was stored in a dry and dark environment until use. Scanning electron microscopy (SEM) was used to determine the size and shape of the synthesized particles. SEM images of nanoparticles A, B and C examined in this work are illustrated in figure 2.1. Particles A are characterized being cubic in shape and crystalline in structure with a diametral size of d = 80-200 nm. Particles B are octahedral in shape and also crystalline in structure. The diameter of these particles was found to be d = 200-300 nm. In contrast, particles C are round shaped and show an amorphous crystal structure. The diametral size of these particles is d = 300-500 nm. The generally wide range of the size distribution is typical for particles synthesized with the precipitation method. A summary of the morphology and size of the particles can be seen on table 2.1.

Table 2.1: CaF_2 nanoparticles A, B and C

	A	B	C
Morphology	Cubic crystalline	Octahedral crystalline	Round amorphous
Diameter (nm)	80-200	200-300	300-500

2.1.2 Sample Characterization and Preparation of Mica and Human Tooth Enamel

Manipulation experiments were performed on mica and teeth enamel as substrate. Both substrates are significantly different. Mica identifies a group of minerals being composed of sheets of silicates, containing silica (SiO_2) as main compound. The mica used in this work is commercially available and very widely used for surface science purposes. It is stable when exposed to moisture and chemically inert. The mica substrate was always freshly cleaved prior to use and is known to have largely extended atomically flat terraces. The teeth substrates used in this work were generously donated from GABA International (Therwil, Switzerland). The sample consisted of in resin embedded human wisdom teeth. Each tooth was mechanically treated with a polishing procedure prior to use. This was needed to remove the biofilm present on natural tooth and to reproducibly get a flat surfaces with comparable surface roughness for all tooth samples. A tooth consists of several layers, the most important in respect to this work, the enamel, the outermost layer of the teeth. On this layer the manipulation experiments were performed. The enamel is the barrier that protects the teeth from

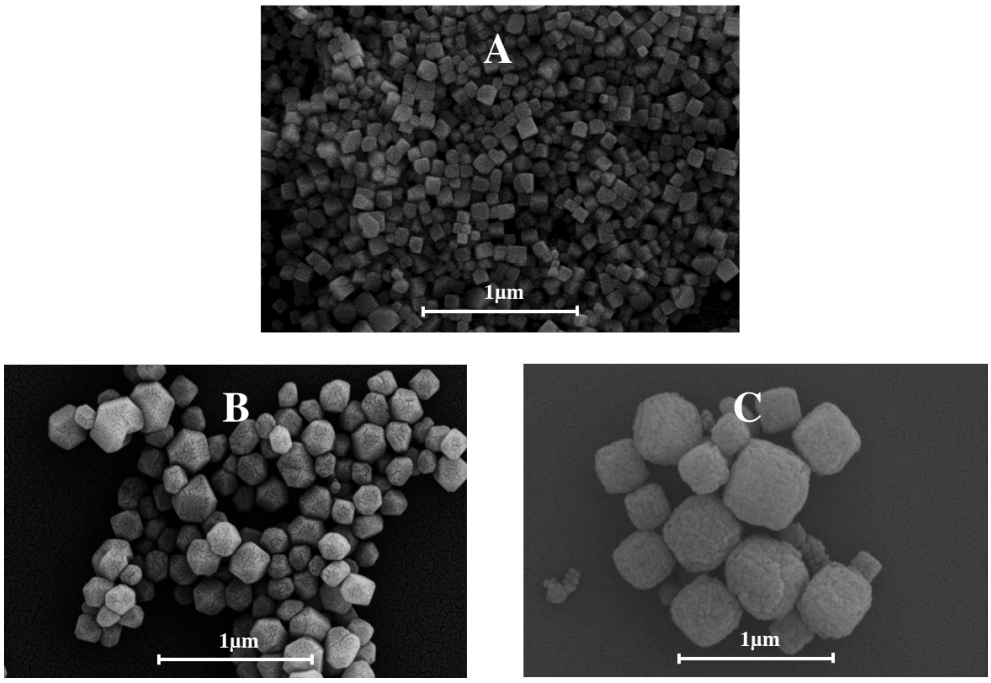

Figure 2.1: SEM images of the CaF_2 nanoparticles explored in this work. (A) shows cubic and crystalline nanoparticles with a diameter ranging between d = 80-200 nm. (B) shows octahedral crystalline nanoparticles with a diameter ranging between d = 200-300 nm. (C) represents round shaped amorphous particles with a diameter of around d = 300-500 nm.

caries attack. It is the hardest substance of the human body has and is build up as a matrix-type of structure. It has the purpose to protect the inner sensitive part of the teeth from physical or chemical attack and to preserve a durable use of the teeth during lifetime. It is composed of 92-94 vol. % of tightly packed fibrous apatite crystals (i.e. crystalline calcium phosphate) which have an approximate diameter of 20 nm [81]. The thickness of the enamel layer is of around 0.8 mm [82]. The teeth were processed prior use with a rotating polishing machine (Knuth-Rotor, Struers, Copenhagen, Denmark). The teeth embedded in resin were first polished with a diamond pasta grain size of 3 μm to remove the irregularities in the surface profile and secondly polished with a 1 μm grain size paste. The polishing procedure was done under constant water cooling, to prevent heating of the sample. After each polishing step the samples were sonicated for 2 min in a detergent solution (2 drops of liquid soap in 150 ml demineralized water) [74]. After the polishing procedure the teeth substrates were analyzed with AFM to verify that the enamel was not fully polished away and to determine the surface roughness. The root mean square roughness (rms) of all teeth used for experiments had a surprisingly mono-disperse surface roughness of rms

= 10-18 nm. The tooth were then stored in a dust-free box and not further processed. In figure 2.2, contact mode AFM topography images done under ambient conditions of two polished teeth substrates are shown. The tooth in 2.2(a) had a roughness of rms = 15.8 nm and clear scratch profiles on the enamel as a result of the polishing procedure. In 2.2(b) a topography image is illustrated where particles A are adsorbed on one of the polished tooth enamel samples. The particles are homogeneously distributed on the tooth at arbitrary places.

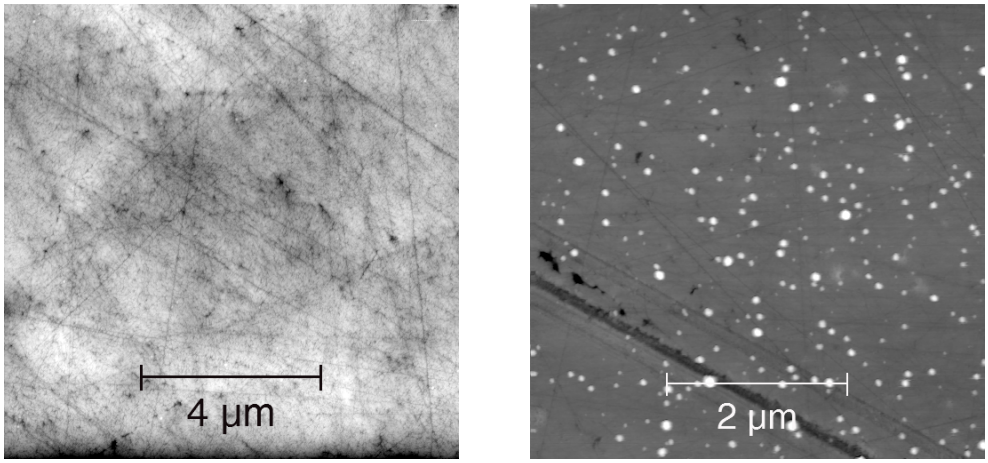

(a) (b)

Figure 2.2: (a) shows a topography image of a polished teeth recorded in the contact mode. (b) shows a topography image of particles A adsorbed on a polished teeth substrate in contact mode imaged under ambient conditions. The particles are seen to be homogeneously distributed on the polished tooth. Imaging conditions: (a) $F_N = 18$ nN. (b) $F_N = 10$ nN.

2.1.3 Manipulation Experiments in Liquid with AM-AFM

All imaging and manipulation experiments were performed using a commercially available AFM (Flex AFM from Nanosurf AG, Switzerland). The microscope was controlled via a control electronic Nanonis from SPECS®. Rectangular silicon cantilevers with typical resonance frequencies in air and liquid of 160 kHz and 70 kHz, respectively and spring constants of 45 N m^{-1} and 7 N m^{-1}, respectively have been used (PointProbe® PPP-NCLPt from Nanosensors AG, Switzerland). To compare the manipulation experiments done on mica and on tooth enamel the measurements were performed with comparable amplitudes and set points. All manipulation experiments were done in liquid in a saturated CaF_2 solution. This ensured that the

nanoparticles did not change in structure or chemical composition during a measuring period. The adsorptions of CaF_2 nanoparticles on the sample surface was performed as follows. An aliquot of the dried nanoparticle powder was mixed with 200 μl of a saturated calcium fluoride solution and put in an ultrasonic bath for 20 minutes to break aggregated particles. 2 μl of this solution was then added to the substrate and waited 20 min to let the particles settle down. The excess of liquid was blown away with a flow of N_2-gas and the teeth immediately covered with large amount of the saturated calcium fluoride solution. All measurements were performed in a saturated solution of calcium fluoride, ensuring that no or minimal changes of the adsorbed nanoparticles occurred during the measurement.

2.2 Imaging of *E. coli* Bacteria

The human body is fully colonized with bacteria, from the skin to the mouth to the gastrointestinal system. These bacteria are essential to humans for many reasons but can become harmful if they pass into blood or blood-circulated tissues. The strategies of how bacterial disease are caused and expressed can be very diverse. For example, the way intestinal bacteria cause a disease can range from adhere to or invade the epithelium or the production of secretory exotoxins or cytotoxins [83]. The human body has different barriers against the bacteria so they can not enter into the blood circulated tissues. These barriers consist of epithelial as well as membranes that are strengthened by layers of collagen and connected to other tissues [84]. The primary barrier against the outside of the world is the mucosal layer. Most infections actually involve the mucosal surface, where the primary secretion against infections is the antibody immunoglobulin A (IgA) [85]. Immunoglobulin A is a human antibody with a molecular mass of around 60 kDa which is produced in the mucosal linings and is by far the most abundant immunoglobulin of all secretions [86]. The antibody IgA has been reported to shield the surface of mucosal lining against pathogenic attack of bacteria [87]. It has been reported that IgA multifunctional regulates the uptake of pathogenic bacteria and allergenic antigens across the intestinal epithelium [88]. An early study has shown that the treatment of *Streptococcus* gram-positive bacteria with a secretory of IgA (S-IgA) inhibited the adherence of these bacteria on epithelial surfaces [89].

One section of this work studies how the immunoglobulin A changes the morphology of native *Escherichia Coli* (*E. coli*) bacteria upon incubation with the antibody. *E. coli* bacteria are known to be important for a normal intestinal microflora but have also been reported to be the cause of diverse intestinal diseases or infections [90]. It has been shown that *E. coli* flagella, i.e. the motor of the cell, is important for the bacteria to cause infections in the urinary tract [91] and that use of an antibody against the flagella could prevent the spread of infections caused by the bacteria in the kidney [92]. We will examine the effect of the immunoglobulin A on the bacteria body and the flagellum with AFM under ambient conditions. The flagellum is known as the motor of certain prokaryotic and eukaryotic cells where its primary use is the locomotion. This motor is about 45 nm in diameter and consists of about 20 different kinds of parts and can spin at a speed of several hundred Hz [93]. Any modification of this "engine" due to IgA resulting in a decreased functionality would affect the mobility these bacteria strongly minimizing the possibility to enter blood circulated tissues and cause an infection.

Imaging of *E. coli* bacteria was done using a commercial available AFM (AFM from Anfatec with the SPM controller AFT-MMC50). Rectangular

silicon cantilever have been used (PointProbe® PPP-CONT and SuperSharp-Silicon® SSS-NCLR both from Nanosensors AG, Switzerland). Supersharp cantilevers with a low tip radius of around 2 nm were used in order to enhance imaging contrast. The contact levers and the tapping levers had a typical normal spring constant in air of around 0.02 N m^{-1} and 45 N m^{-1}, respectively. Native and IgA incubated bacteria were obtained from the group of Prof. Dr. Andrew Macpherson by Dr. Li Hai from the University of Bern (Department of Gastroenterology and Mucosal Immunology). The bacteria were provided in a buffer solution (PBS - Phosphate Buffered Saline where the osmolarity and ion concentrations of the solution are close to those in the human body enhancing the living time of the bacteria. 50 μm of the bacteria solution were centrifuged for 3 min at 6000 rpm. The excess of liquid was then sucked away and 50 μm of distilled water was added and the flask again centrifuged, this was repeated 3-times. This procedure was needed to get rid of most proteins and salts present in the solution as we wanted the bacteria to be as free as possible from proteins and salts when we adsorb them on the sample substrate. A drop of the bacteria was then transferred to a piece of a silicon wafer and let dry. All measurements were done under ambient conditions.

2.3 Magnetic Bacteria Analyzed with AFM

Magnetotactic bacteria (MTB) were first introduced to the scientific community by Blakemore [94]. They are of a group of bacteria which have magnetic nanoparticles incorporated in their body to orient via sensing the earth's magnetic field used to find optimal living conditions [95]. MTB favor to live in so-called anoxic waters, which are found in layers close above the sediments in slow current waters. It has even been reported that MTB are able to maintain their position at their preferential oxygen concentration using the combination of magnetotaxis and aerotaxis [96]. The mechanism of animals using the physics of magnetism for navigation is called magnetotaxis. As magnetotaxis, one precisely understands the ability of living organisms to orientate along the earth's magnetic field via internal magnetic structures, called magnetosomes [97]. Magnetosomes are a membranous structure which consists of cubooctahedron nano-magnetite, either magnetite Fe_3O_4 ($Fe^{\mathrm{II}+}(Fe^{\mathrm{III}+})_2O_4$) or greigite, where simply the oxygen is replaced by a sulfur atom. These anorganic iron minerals are synthesized by the bacteria themselves in specific organelles present in the magnetosomes [98]. The bacteria have full control over the construction, shape and size of each single magnet used to build up a chain with a stable oriented magnetic moment [99]. The size of these nanomagnets is found to range between 30-50 nm in diameter. In figure 2.3 a SEM image of a magnetosome chain consisting of these single ferro-nanomagnets from the *Magnetospirillum gryphenwaldense* bacteria species is shown. These highly pure biogenically produced nanomagnets of the MTB, have called attention to the scientific community as they have a wide range of application, from data recoding [100], to medical applications in drug delivery [101], magnetic imaging resonance MRI for contrast enhancement [102] to hyperthermal cancer therapy [103]. Iron containing minerals are known to have size dependent magnetic properties. Magnetite particles with diameter size between 35-80 nm are likely to be single-domain magnets [104] where size thresholds about 20-30 nm exhibit superparamagnetic behavior at room temperature [105, 106].

AFM and MFM imaging of extracted magnetosome chains has already been performed [107]. Another study reported a single-domain magnetic particle from extracted magnetosome in a trout [108]. A decreased coercivity and reduced remanence was observed for extracted magnetosomes compared to intact ones [109]. Several approaches have been taken to explore the magnetic properties of intact magnetosomes. Electron Holography was applied to give high resolution images of the local magnetic stray fields of nanomagnets in the magnetosomes of intact *Magnetospirillum magnetotacticum* bacteria species and they concluded a magnetic moment of one specific chain to be 7×10^{-16} A m^2 [62]. Gysin *et al.* [61] performed can-

tilever magnetometry measurements at room temperature with about 100 randomly oriented MTB and deduced an average magnetic moment of 5×10^{-16} A m^2. Also the dynamic properties of MTB in a rotating magnetic field have been investigated experimentally and theoretically [110]. One main goal of this thesis is to examine the magnetic properties of a **single** MTB of the species *Magnetospirillum gryphenwaldense* with dynamic cantilever magnetometry.

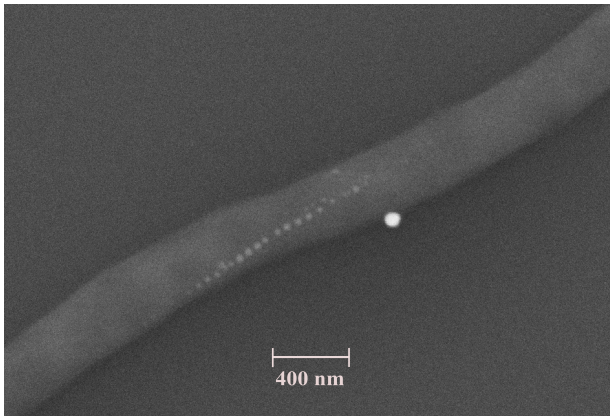

Figure 2.3: TEM image of a magnetosome chain from the *Magnetospirillum gryphenwaldense* bacteria species. The ferromagnetic nanomagnets are arranged in a pearl necklace way along the longitude of the bacteria body. Each nanomagnet is embedded in a membranous structure and spaced from the neighboring magnets.

2.3.1 Superparamagnetism, Single-Domain and Multidomain Nanomagnets

The magnetotactic bacteria are known to have full control over the shape, size and crystal structures of the synthesized magnets, tuning the magnetic properties of the magnetosome chains in such a way that they are optimally adapted to the environment they are living. The magnetic properties of nanomagnets strongly depend on the size and crystal structure [111]. Different sizes of the nanomagnets cause the particles to be either in the superparamagnetic (SP), single domain (SD) or multidomain (MD) state. In case of a SP state, the particle is not able to maintain a stable magnetization at room temperature, the magnetization continuously alters due to thermal fluctuations of the spins. At at temperature of 5 K (well below the Curie temperature) the SP state becomes ferromagnetic where the magnetization is not altering thermally. The magnets in the magnetosome chains of MTB are known to be in the SD state [112]. In this state the magnetic dipoles of the magnets are all aligned parallel forming an uniform magnetization.

The resulting magnetization is then a maximum for a given volume. For particles in the MD state, a stable uniform magnetization does not occur, as neighboring domaines can have distinct polarity. For this reason magnetotactic bacteria or any organism using magnetotaxis produce magnets in size and structure which are in the SD state, where the magnetization and the remanent magnetization is much enhanced in respect to particle in the MD or SP state [113].

In the next part, we will explain how the bacteria were chemically treated enabling imaging of the magnetosome chains of magnetotactic bacteria with AFM. In a second part we will discuss how a single bacterium was successfully transferred on an ultra-sensitive cantilever. The last section will explain in detail the experimental set up of the cantilever magnetometry measurement performed on one single MTB.

2.3.2 Chemical Treatment of Magnetic Bacteria

To be able to image the magnetosome chains with AFM under ambient conditions, the bacteria had to be treated with a chemical solution prior imaging. This treatment of the bacteria resulted in shrinking of the cells, enabling the tip to sense the magnetosome chain. An ethanol solution saturated with NaOH was used to pinch the membranes of the bacteria. A small drop of the bacteria, which were suspended in distilled water, was put on a clean piece of a silicon wafer where a strong permanent magnet was placed below. After 5 min the excess of liquid was gently blown away with a flow of N_2-gas and only the magnetosome containing magnetic bacteria remained at the surface as they where hold on place by the magnet. The sample was immersed in an ethanol solution saturated with NaOH for 15 min. The excess of liquid was again blown away with a flow of N_2-gas, followed by multiple rinsing with deionized water. The sample was directly used for imaging under the AFM. Upon treatment of the bacteria, the mean thickness of the bacteria decreased from 300 nm to approximately 150 nm, providing enough closeness of the tip to image the magnetic chains.

2.3.3 Sample Preparation

The main problem to perform cantilever magnetometry measurements of one single magnetotactic bacteria, was to transfer a single bacterium with length of about 4 μm on a tip-less cantilever. For this purpose we used a home-build micromanipulator, where the glue and the single bacterium was picked up and transferred to the tip-less cantilever with femtotips (Femtotips® from Eppendorf). First, a drop containing intact non-chemically treated magnetotactic bacteria was transferred to a Teflon covered sample plate which had a permanent magnet below. After 10 min deposition time,

the excess of liquid was blown away with a flow of N_2-gas, where only bacteria containing magnetosomes were left-behind. A single bacterium was then picked up with a femtotip and transferred to a cantilever which had an UV-glue covered free end. We used an UV-glue to have the possibility to properly align the bacterium on the cantilever, minimizing the misalignment of the magnets relative to the external applied magnetic field before hardening the glue. The hardening of the glue was then done after exposure to UV-light for 2.5 h. SEM images of single MTB bacteris glued at the free end of an ultra-sensitive tip-less cantilevers are illustrated in figure 2.4.

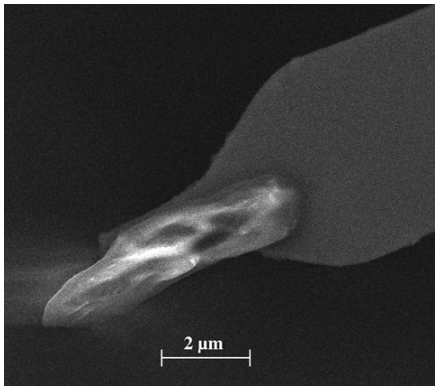

(a) Single magnetotactic bacterium attached on a tip-less cantilever with UV glue.

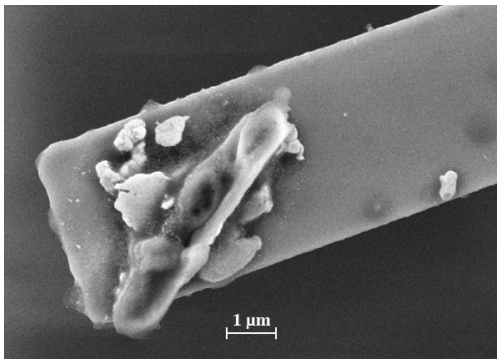

(b) Single MTB fixed on a tip-less cantilever with epoxy glue.

Figure 2.4: (a) SEM image of a single magnetotactic bacterium glued at the free end on an ultra-soft tip-less cantilever. The length of the bacterium is around 4 μm, which is the length of a single bacterium. The spring constant and resonance frequency could not be determined as this specific cantilever broke during transfer to the microscope. In (b) an other SEM image of a single glued MTB at the end of a cantilever is visible. This cantilever had a length of $L = 450$ μm, width of $w = 4$ μm, a thickness of 0.35 μm, resulting in a spring constant of $k_N = 95$ μNm^{-1} and a resonance frequency of $f_{res} = 2500$ Hz.

2.3.4 Methods of Dynamic Cantilever Magnetometry

The cantilever magnetometry measurements were done in a system described in detail in this publication [114]. The cantilever was driven in the first flexural eigenmode using a piezo-actuator. The frequency response of the cantilever depending on the magnetic field, was demodulated with a completely digitized phase-lock-loop (PLL) electronic circuit. The demodulation bandwidth of the PLL was 0.1-1 Hz for submicrohertz frequency resolution. A superconducting magnet was used to generate the desired

magnetic fields (up to ± 7 T). The experiments were done in UHV at a temperature of 5 K. The cantilevers used were custom designed ultra-sensitive tip-less cantilevers [115].

Chapter 3

Results and Discussion

3.1 Calcium Fluoride Nanoparticle Manipulation in Liquid

All data presented in this section were obtained while measuring in liquid in the AM-AFM mode, in a saturated solution of calcium fluoride. Compared to measurements under ambient conditions, manipulation experiments in liquid have the advantage that the retention of adsorbed particles is not dominated by the wetting layer (hydrodynamic drag of water layer), but the intrinsic particle-sample interaction forces. The dissipated power at the point of particle manipulation was used to examine the retention properties of these particles in respect to the particle-sample contact area and the chemical affinity between them. We used the same set points and free amplitudes for all experiments enabling comparable results. In a first part, we will show that the dissipated energy from the tip at the point of particle manipulation is directly used to dislocate the nanoparticles. Manipulation experiments on atomically flat mica will show that the trajectory angle of the manipulated particles is proportional to the particle-substrate contact area. In a last part, a comparison is made between the retention properties of CaF_2 nanoparticles adsorbed on mica and on polished tooth enamel. There we will examine the influence of the sample surface roughness on the mobility of these particles. We will show that the chemical interplay between the adsorbate and the substrate (i.e. particle-substrate interaction) greatly influences the particles retention properties.

3.1.1 Relation between Trajectory Angle and Dissipation

To relate the dissipated power of the tip at the moment of particle manipulation to the intrinsic retention properties of the calcium fluoride nanopar-

ticles, i.e. the particle-substrate contact area and the chemical interplay between the particles and the sample, the phase-lag at this point was recorded. The resulting trajectory angle was then used to determine the particle-sample contact area. In figure 3.1(c) a phase image of particles (A) adsorbed on mica is illustrated, where θ correspond to the angle of the manipulation direction and the values 1 and 2 to the two particles that have been manipulated. The corresponding phase-drops for particle 1 and 2 can be seen in 3.1(b). The manipulation of particle 1 resulted in a phase-drop of $\Delta\varphi$ = -5° and an angle of deflection $\theta = 65°$. The phase-drop is negative as the tip-sample force was dominated by a net repulsive force, where $\varphi < 90°$. In case of particle 2 being manipulated, a phase-drop of $\Delta\varphi$ = -14° and an angle of deflection equal to $\theta = 75°$ was observed. A higher phase-drop correlates with a higher angle of particle deflection. As the magnitude of the phase-drop is related to the energy dissipation, this means that for particles with a high particle-substrate contact area more energy was delivered from the tip to the particles to induce dislocation. Figure 3.2 is a plot of the calculated dissipated energy versus the radial contact area calculated from the deflection angles via Eq. (1.7) for particles (A) adsorbed on mica. In case of particles with a plane surface structure, adsorbed on atomically flat mica, the contact area equals to a close proximity to the size distribution of the adsorbed particles. A radial contact area of 40-200 nm is observed which is in very good agreement with the size distribution of the particles observed on the SEM images. Graph 3.2 also gives indication about how the particles where adsorbed (i.e. single particles and size of the conglomerates). In this specific experiment, particles (A) showed a low tendency to be adsorbed as conglomerates. We can conclude, that for particles with a plane surface facing adsorbed on a atomically flat substrate, the deflection angle of the manipulated particles correlates with a larger particle-substrate contact area and hence with a higher energy to dislocate the particles. The oscillation energy from the cantilever tip can be regarded as being directly transferred to induce manipulation of the particle. It also shows that for particles with a higher contact radii, more energy is needed to induce displacement.

3.1.2 Dissipation Histograms for Different Nanoparticles

In the previous section, we showed that the recorded phase-lag and hence the dissipated energy is proportional to the deflection angle for particles with smooth and plane facets adsorbed on a flat substrate. In this section we will compare the obtained energy dissipation histograms for the different nanoparticle (A), (B) and (C) when adsorbed on mica. The energy

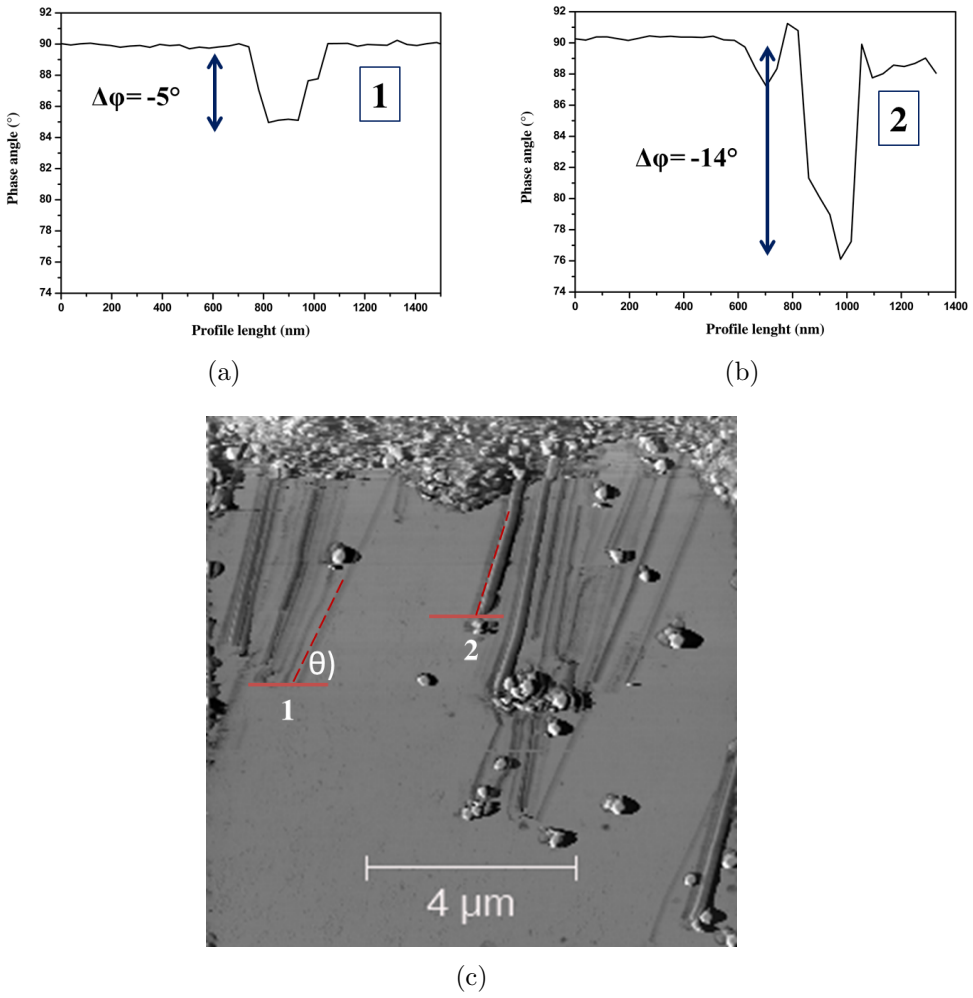

Figure 3.1: (a) and (b) show the phase-drop line scan at the point of particles manipulation at position 1 and 2. (c) Is the corresponding phase image, showing the two position of particles manipulation and how the deflection angle θ is evaluated. A lager phase-drop correlates with a larger deflection angle. Imaging conditions: f = 66.32 kHz, A_0 = 15 nm, Set pt.= 90 %.

dissipation histograms obtained for the three nanoparticles are illustrated in figure 3.3. Specimen (A) and (B) are cubic and octahedral, respectively and both show plane and smooth surface facets. Whereas specimen (C) is round shaped and has amorphous and rough facets. Considering the retention to be determined by the particle-substrate contact area, we expect to measure the lowest dissipated power for particle (C). Indeed, the distribution of the dissipated energies is lowest for the specimen (C), with peaks between $\overline{P_{tip}}$ = 1-5 keV/cycle. The rough and spherical surface structure of these particles strongly minimizes the area of contact with the substrate

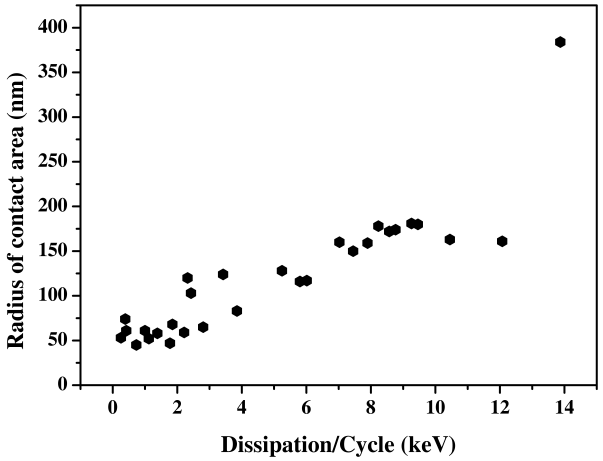

Figure 3.2: Plot of the dissipated energy versus the radius of the contact area of the nanoparticle for species A adsorbed on mica.

due to a decreased number of contacting asperities in the interface of the nanoparticle-substrate contact zone. For specimen (A) we find a sharp peak of the power dissipation at $\overline{P_{tip}} = 1$ keV/cycle and further multiple peaks up to 14 keV/cycle. The precipitation method used to synthesize these particles generates a certain size distribution, which is seen in these multiple peaks in the power histogram at elevated energies. The high power peaks up to 14 keV/cycle are due to the fact that also conglomerated particles have been manipulated. For specimen (B) we find a large number of peaks up to 19 keV/cycle. Nevertheless, we find the dissipated power values to be comparable with the ones for specimen (A). Although particles (B) are bigger in size, their octahedral morphology results in a comparable surface area of the particles to make contact with the substrate as for specimen (A). The spread in the dissipated power is most probably a result of a higher tendency of these particles to conglomerate.

In this chapter, we have shown that for particles adsorbed on a flat substrate like mica, the smaller particles with a diameter ranging from 80-200 nm with a smooth and plane surfaces show higher retention as big particles with a diameter of 300-500 nm with rough and spherical facing. We find that the particle-surface contact strongly depends on the surface facing of theses particles when they are adsorbed on a flat and chemically inert substrate, like on mica.

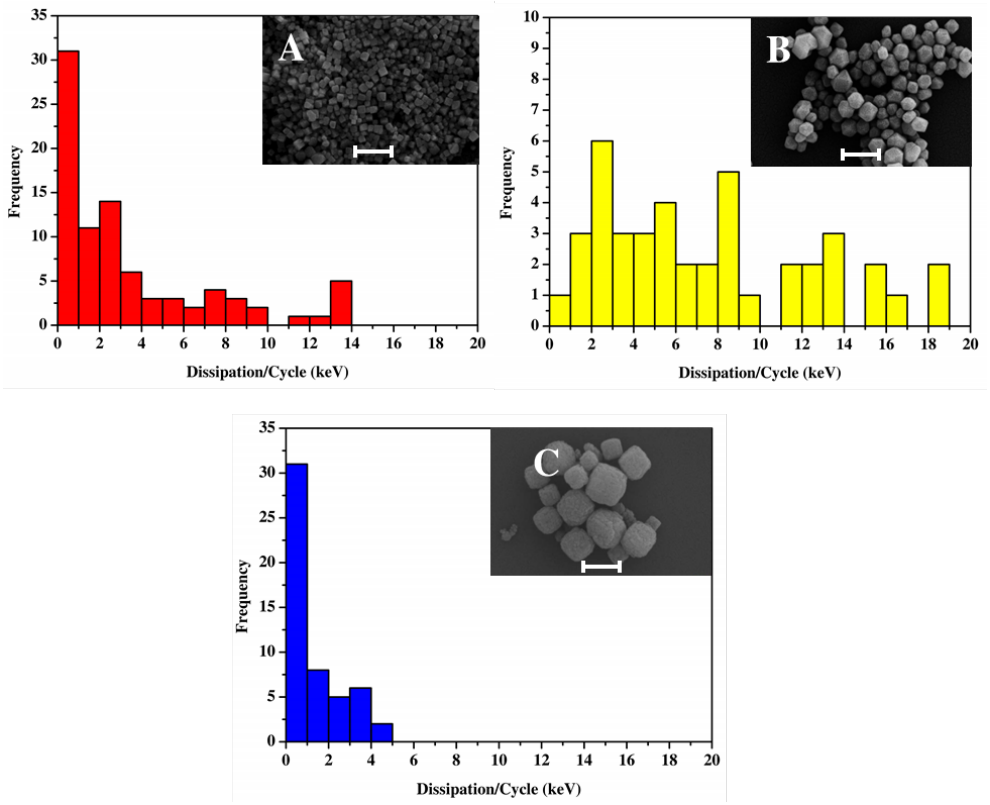

Figure 3.3: Dissipation power histograms obtained for nanoparticles A, B and C adsorbed on mica. The dissipated power is strongly related to the size distribution of the adsorbed particles and their surface facing creating contact with the substrate. The bar on the inset SEM images showing the nanoparticles corresponds to 1μm.

3.1.3 Comparison of Dissipation Histograms on Mica and on Tooth Enamel

We have already discussed the power dissipation histograms when the calcium fluoride nanoparticles are adsorbed on mica. In this section, we will discuss how the histograms look like when the particles are adsorbed on polished tooth enamel. To compare the results it is important to know the difference between both substrates. The main differences are the obvious different chemical composition and the surface roughness. Where mica is known to be atomically flat and chemically inert, the mechanically polished teeth substrates showed an average surface roughness of rms $\approx$ 13 nm.

The histograms in figure 3.4 show the distribution of the calculated power dissipated for the three nanoparticles (A), (B) and (C) adsorbed on mica (a) and on the polished tooth enamel (b). At first sight, we see that the energy dissipation for each of the particles is found to be much higher

on enamel than on mica. For particles (A) and (B) we get up to 5-times higher and for particles (C) up to 8-times higher retention when adsorbed on tooth substrate. Further, we also observe that the peaks of the histograms measured on the teeth substrate are more widely distributed. This is an effect coming from the inhomogeneous scratch profiles for each of the used polished tooth enamel substrates, as this is seen for all three particles. The highest retention is observed for particles (C), which might arise from the fact that the rough surfaces facing of these particles created an interlocking between substrate and particles increasing the particle-surface contact and hence the power needed to dislocate them.

The interaction between a particle and a substrate is known to depend on the size of the contacting area, i.e. the nanoparticle- and substrate surface roughness and geometry. Compared to mica, the tooth enamel has substantially larger surface roughness. An early study showed that the surface roughness has an effect on the contact area of solids [116]. If we assume the retention to be only contact area dependent, the higher substrate roughness of enamel would lower the particle-substrate contact area and hence the power needed to induce particle dislocation. Former experiments have shown, by measuring the pull-off force of nanoparticles attached to a cantilever tip on differently rough surfaces, that the adhesion strength is reduced on rough surfaces [117, 118]. Recent studies have also simulated that the mobility of nanoparticles is enhanced on rough surfaces, compared to smooth ones, if the asperities are much smaller than the particles [119, 120]. This phenomenon was explained in terms of less contacting asperities in the substrate-particles interface and hence less adhesion force acting in between them. The above presented experiments show the exact opposite behavior. The higher substrate roughness the larger retention of the nanoparticles is observed. A higher lateral mobility of particles on rough surface may also come from interlocking of particle asperities with the grooves of the substrate. For particles (C), which has a rough surface, this might contribute to the higher retention, but for the other two nanoparticle which had a smooth facing an interlocking can not be assumed. The mobility of adsorbed particles on one side depends strongly on the number of contacting asperities but also on the chemical interaction forces acting between both. For the tooth enamel which is highly rough compared to the atomically flat mica, the increased retention observed for the calcium fluoride nanoparticles is a result of the positive chemical interplay between substrate and adsorbate. In this case, the chemical forces are so strong that they can compensate the reduced number of contacting asperities. This finding that the chemical interplay between the calcium fluoride and the tooth enamel is so strong in respect to their adhesion strength, is very promising, as these particles are to be incorporated in dental care products as anti-caries agents.

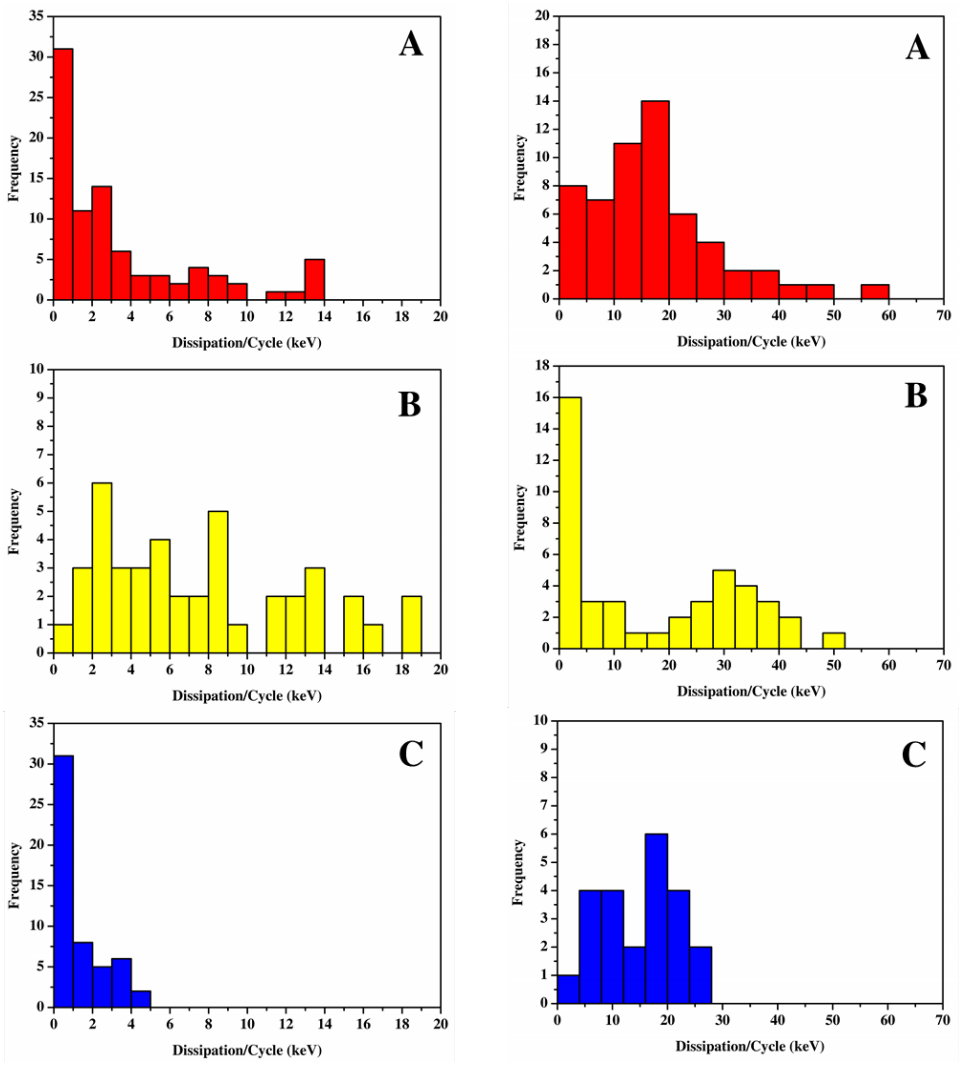

Figure 3.4: (a) shows the histograms of the dissipated energy for particles absorbed on mica as substrate. (b) shows the histogram for particles adsorbed on polished tooth enamel as substrate. For particles A and B an increase in energy to induce manipulation of around 5-times on tooth enamel compared to mica as substrate is observed. Particles C, show 8-times higher retention on the tooth substrate. The large spread of the dissipation peaks seen on the teeth substrates are an artifact of the inhomogeneous scratch profile of the used enamel samples.

3.1.4 Summary

In conclusion, first we have performed manipulation experiments on a flat substrate like mica. From the phase-lag at the point of particles manipulation we were able to determine the power that was transferred from the

tip to the particle inducing manipulation. The deflection angle relative to the fast scan axis was read out to determine the particle-substrate contact area. We showed that the phase-drop strongly relates to the deflection angle, concluding that the retention of calcium fluoride nanoparticles on a flat and inert substrate like mica is exclusively contact area dependent. In the second part, we examined the effect of the surface roughness and the chemical composition of the substrate to the retention properties of calcium fluoride nanoparticles. We showed that for nanoparticles adsorbed on the rough tooth enamel, which had a rms $\approx$ 13 nm, more energy was needed to manipulate the particles compared to those adsorbed on mica. We interpreted this finding as a result of the strong chemical interplay between the calcium fluoride and the enamel, compensating for the reduced number of contacting asperities. We have shown that calcium fluoride nanoparticles are a suitable candidate, in respect to their adhesion strength, to be used as an additives in dental care products reducing caries [121].

3.2 Imaging of *E. coli* Bacteria

To examine the effect of the antibody immunoglobulin A on the morphology of *E. coli* bacteria, the force modulation microscopy (FMM) was used. In FMM in addition to contact mode images, which give information about the frictional properties of the substrate, we acquire amplitude and phase images which directly correlate to the stiffness of the contact. The amplitude and phase images obtained from the contact resonance also show a higher contrast compared to normal AM-AFM images. The operating mode will be indicated on all images.

3.2.1 Influence of the Antibody IgA on the Morphology of *E. coli* Bacteria

In figure 3.5, topography images of native *E. coli* bacteria (a) and antibody IgA incubated bacteria (b) obtained in the FMM mode are illustrated. Two observations from those images: most cells are damaged and the bacteria incubated with IgA show less damage and are highly uniform in shape compared to the native ones. In experiments done under ambient conditions, where the drying is part of the bacteria preparation procedure, it has been reported that the locally increased peptide concentration upon drying may cause a damage to an unaffected cell or increase the damage of an already damaged cell [122]. The blue circles mark damage at the apical ends of the cells, where on both images we see a collapsed and flattened area of the cell, most probably as a result of the drying procedure. The yellow circles on the image 3.5(a) show other kind of cell lesions at arbitrary places on the bacteria. For the IgA incubated cells, damage of the bacteria body is observed at the apical ends, whereas for the native ones lesions at any position on the cell occur. This lesions normally cause the release of a large amount of vesicles and proteins. Release of cell liquid (cytoplasma) is a proof that the inner cell membrane of the cells was hurt. Despite these lesions, the IgA incubated bacteria are able to maintain their cell shape and morphology and show a smooth structure of the body. The antibody IgA seems to prevent the bacteria from collapsing, like if the antibody is protecting the bacterial body like a shield. The opposite is observed for the native bacteria, where their shape and structure is highly influenced after the drying procedure. Native bacteria also show pore-like lesions and grooves (dark areas) on the cell body, indicating that large amount of material from the inside of the cell was released. It was always difficult to get a stable imaging contrast on native *E. coli* bacteria which might be related to pinning of the membranes (at arbitrary positions on the cell) upon being dried causing the release of a high amount of vesicles and proteins, polluting the tip and hence making it difficult to obtain good resolution. On both images we also observe dif-

ferent stages of bacteria cell division. In figure 3.5(b) one can see bacteria just starting to divide (number 1) and cells which are already in the final stage of division. Those are bacteria which are in a head-to-head position (number 2). The flagella, i.e. the engine of the bacteria, is visible for some bacteria as the "rod" like structure at the bottom of the surface. The most evident effect of IgA on *E. coli* bacteria so far is, that the morphology of incubated bacteria is preserved upon drying.

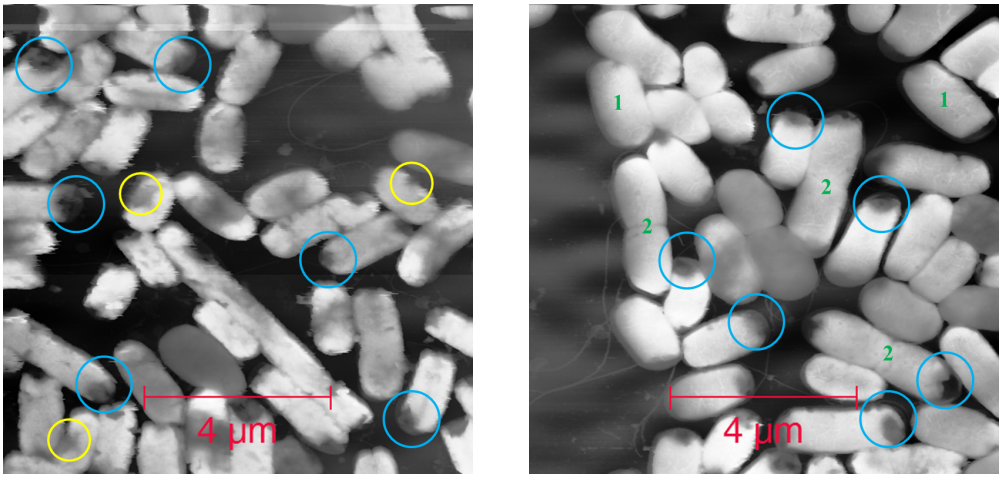

(a) (b)

Figure 3.5: Topography contact-tapping mode images of native *E. coli* bacteria (a) and with antibody IgA incubated (b) bacteria. The blue circles just show some examples of lesions at the apical ends of the cells. The yellow circles show some examples of lesions at any other position on the cells. Number 1 shows cells who have just started cell division, seen as thicker cells, where number 2 shows cells who just finished cell division. Imaging conditions: (a) f_{cont} = 59.3 kHz, F_N = 9.2 nN. (b) f_{cont} = 56.5 kHz, F_N = 7.1 nN.

In figure 3.6, high resolution images taken in the FMM mode for native *E. coli* bacteria (a) and IgA incubated bacteria (b) are shown. Inhomogeneous morphologies are observed for the native bacteria compared to the incubated ones which was already discussed in detail above. In the amplitude and especially in the phase image of 3.6(a), change in the phase contrast for the material surrounding the cell, clearly indicates the loss of vesicles, proteins and membrane associated compounds (orange rings). Such phase contrast is also observed for the incubated bacteria, however less pronounced. In figure 3.6(b), a "ring" is surrounding the cells, thus implies the loss of a large amount of fluid from the cell during the drying procedure [123]. Beside the damages of the cells while drying the bacteria, both species show an obvious "worm"-like structure covering the outermost membrane of the cell. This structure is very strongly pronounced on the in-

cubated bacteria. Analysis of the surface structure of native *E. coli* bacteria performed in the past, has attributed this surface features to lipopolysaccharide (LPS) molecules and has been found to be the major component of the outer membrane of gram-negative bacteria like *E. coli* [124].

Table 3.1: *E. coli* surface roughness

	Non-IgA	IgA
Surface roughness (RMS)	$3.5 \pm 1.3\ nm$	$5.7 \pm 1.5\ nm$

In table 3.1, the surface roughness of native and IgA incubated *E. coli* bacteria is shown. The analysis of the surface roughness for incubated bacteria gave $R_{rms} = 5.7 \pm 1.5$ nm and for the native cells $R_{rms} = 3.5 \pm 1.3$ nm. In comparison, the surface roughness of intact *E. coli* bacteria was reported in the literature to be in the range of 2.4 ± 1.42 nm [122] and 2.5 ± 0.3 nm [125]. The surface roughness of the native bacteria is found to be slightly higher than the literature values, which can be explained by the fact that the high degree of damage of the cells after the drying procedure resulted in shrinking of the cell body affecting the surface roughness. Nonetheless, the surface roughness of the incubated *E. coli* is found to be 2 nm higher than the value for the native bacteria. This is expected, regarding the fact that the grooves and "worm" like structures are more pronounced on the incubated cells.

The obvious changes in the morphology for native and incubated *E. coli* bacteria have been discussed above. What is missing so far is the statistical analysis of the sizes of the bacteria which could be attributed to the presence of the antibody IgA. The statistical determined widths and heights of the bacteria and the flagellum are shown in table 3.2 and table 3.3, respectively. Analysis of the bacteria and flagellum sizes were determined from more than 40 bacteria, excluding bacteria which were in a stage of cell division. The width of the bacteria is in the range of around 1 μm. A standard deviation of around 13 % was obtained for the native *E. coli*. Mostly due to the high number of lesions causing a high spread of the measured width values. The height distribution somehow does not show a similarly large variance. This indicates that the lesions caused a shrinking of the bacteria due to loss of cytoplasm (i.e. cell liquid), while the cytoskeleton (i.e. the cells framework) remained unaffected and prevented the cell from totally collapsing. For the incubated bacteria we get similar values of the width as for the native bacteria, however the standard deviation is much smaller compared to the value of the untreated bacteria due to less lesions. This was expected as the incubated *E. coli* showed less lesions. The height of both bacteria types is in the range of around 150 nm and comparable for both species. Regarding the statistics of the height and width we do not see any obvious difference

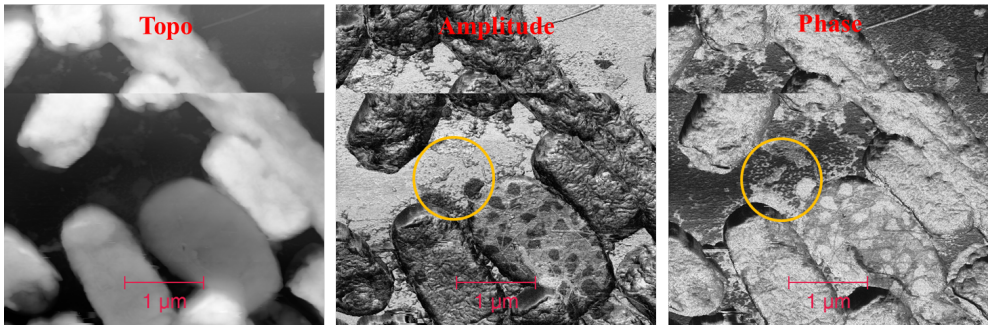

(a)

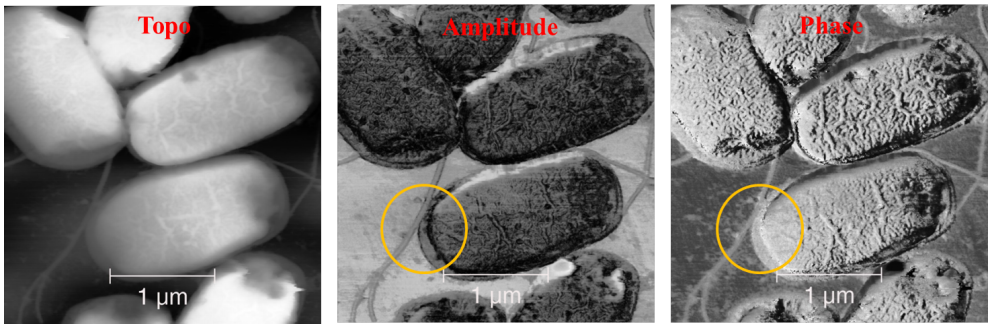

(b)

Figure 3.6: Contact-tapping images obtained for native *E. coli* bacteria (a) and with the antibody IgA incubated ones (b). The orange rings just highlight regions where the loss of cell material is seen as a result of cell damage. Imaging conditions: (a) f_{cont} = 58.8 kHz. F_N = 8.2 nN. (b) f_{cont} = 55.3 kHz. F_N = 6.8 nN.

between the values which can be correlated to the presence of the antibody IgA. The differences are in the range of the error.

Table 3.2: *E. coli* bacteria size

	Non-IgA	IgA
Width (FWHM)	1116.2 ± 150 *nm*	1070 ± 38.7 *nm*
Height	158.8 ± 26.3 *nm*	142.3 ± 14.9 *nm*

Now, we will discuss the statistical values obtained for the flagellum. The width for both cases lies in the range of approximately 60 nm. The width of the flagellum was found to be 2 nm higher for the native *E. coli* compared to the incubated ones. A decreased thickness of the flagellum is observed after incubation with IgA. The height value for the flagella are in the range of around 6 nm, whereat the difference is within the error.

Concerning the sizes of the flagellum and the bacteria for IgA incubated and native *E. coli* bacteria, the difference lies within the error bars, besides the width of the flagellum. One might assume that the antibody IgA immobilizes the bacteria due to change of the flagellum, i.e. the motor of the bacteria. If it would get thicker, due to binding of the antibody, the increase in mass would lead to an increased inertia and hence reduce the power of motion of the bacterium. The statistical data show the opposite effect of IgA on the flagellum. This could indicate that the antibody modifies the flagellum somehow influencing its functionality as a molecular motor. Further studies have to be performed to clarify the exact effect of IgA on flagellum.

Table 3.3: *E. coli* flagellum size

	Non-IgA	IgA
Width (FWHM)	64.8 ± 2.4 nm	50.3 ± 8.7 nm
Height	6.6 ± 0.5 nm	6.9 ± 0.6 nm

3.2.2 Amplitude Bistability on IgA Incubated Bacteria

In the previous sections the changes in morphology of the bacteria and the flagellum upon incubation with the antibody were discussed in detail. We have shown that the bacteria surface is rougher after incubation and that the bacteria body is less affected by the drying procedure. The substantial increase in stability of the bacteria body to do not collapse upon drying, could mean that the IgA is covering the whole body of the bacteria. This section will show where exactly the antibody is found on the bacteria. We will use AM-AFM images which show amplitude bistability behavior to predict where the antibody can be found on the bacteria. In figure 3.7(a), a typical amplitude vs tip-sample distance curve without bistability is shown, where the amplitude drops linearly with decreasing tip-sample distance, and next increases when the tip is retracted. This spectroscopy was recorded over a non-incubated bacterium. Figure 3.7(b) shows the amplitude response for a tip when an amplitude bistability occurs. This spectroscopy was taken over a bacterium incubated with the antibody IgA. First the amplitude drops linearly up to a distance Z = -6.2 nm, where the amplitude suddenly increases 1.5 nm. This self-amplification of the amplitude is caused, because the tip senses a net attractive force during an oscillation cycle, although it is in intermittent contact with the surface. In this case, the amount of repulsive force is small compared to the time it senses the

attractive force [126]. After surpassing this point the amplitude again decreases linearly with decreasing tip sample separation although staying in this high amplitude state. When the tip is next retracted, at a distance of Z = -3.8 nm again a discontinuous jump in the amplitude is observed, but now the amplitude drops 1.5 nm. Forward and backward sweeps then draw a hysteresis loop. Both spectroscopies were taken at the same free amplitude of $A_0 = 7$ nm and at a frequency of $f = f_0 = 183.2$kHz. The spectroscopy recorded on the incubated bacteria indicates the coexistence of two stable cantilever oscillation states. Up to a set point amplitude of $A_{sp} > 5.8$ nm the system is operating in the attractive regime while for set-points values $A_{sp} < 4$ nm the cantilever is operating in the repulsive regime. In between these set points the transition occurrence is strongly enhanced. Whether there is a transition between these two oscillating states strongly depends on the damping of the system [127]. The damping in return is strongly depending on the material properties (i.e. deformation of the sample), where the transition probability is strongly enhanced for compliant samples, like for example biomolecules. Our data show that over a bacterium incubated with the antibody IgA a high tendency of the tip exists to cross discontinuously between both oscillating states. Typically, the system has the tendency to stay in a certain branch of the oscillation state and a nonlinear perturbation is needed to break this tendency and induce bistability. Soft materials, like a body covered with flexible macromolecules, experience a large deformation under contact of the tip, where as a consequence the net force can be negative although the tip is intermittent contact with the surface. Stiff samples and small amplitudes lead to very small contact time and hence give rise to large repulsive forces − net positive forces. A perturbation leading to bistability switching might be due to the IgA molecules. It was already shown that very strong bistability effect is present on IgG (half of IgA molecule) antibody deposited on mica under ambient conditions [49]. The adhesion force, the elastic response and the stiffness change upon adsorption of IgA can perturb the system in a way that amplitude bistability occurrence is strongly enhanced, although the set point were set properly.

In figure 3.8(a), topography and phase images of IgA incubated bacteria are shown. Particularly, in the phase image a strong change in contrast from bright to dark as a result of amplitude bistability is observed. Each of this phase-drops are result of the compliant material properties of the adsorbed IgA antibody. The motion of the cantilever oscillation is perturbed in such a way that the tip-sample interaction force changes from either being dominated by a net attractive or a net repulsive tip-sample force gradient. The stronger the phase contrast, meaning also the magnitude of the amplitude jump, the more the motion of the tip has been perturbed by

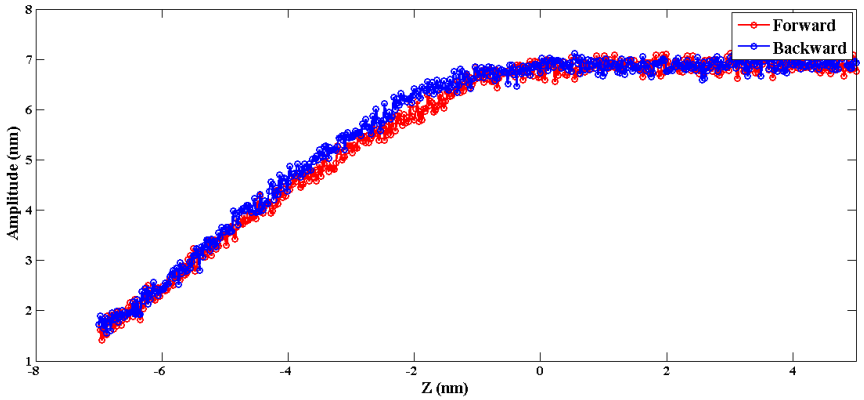

(a)

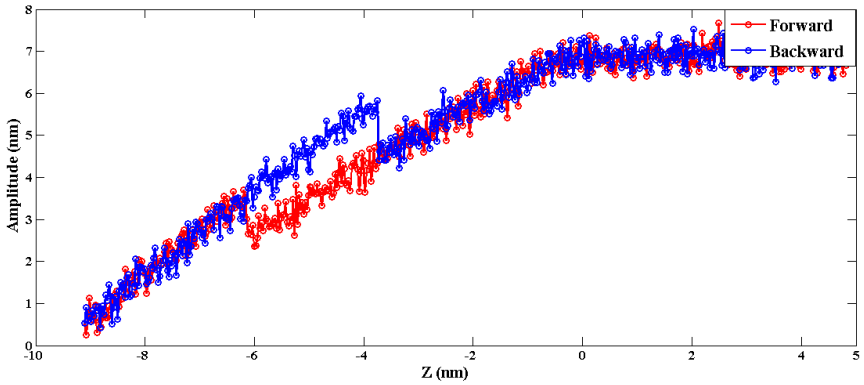

(b)

Figure 3.7: (a) Amplitude vs distance curve taken on a native *E. coli* bacterium, where the amplitude drops linearly with decreasing tip-sample separation. Figure (b) shows the amplitude when the spectroscopy is done over a bacterium incubated with the antibody. A clear discontinuous jump in the amplitude and the hysteresis loop between forward and backward sweeps is seen. The cantilever oscillation frequency was $f = f_0 = 183.2$ kHz and the free amplitude for both $A_0 = 7$ nm.

nonlinear tip-sample interaction [127]. At a first sight, a strong change in contrast on certain parts of the bacteria body, specially on the flank of the cell is seen. Remarkably, the overall contrast changes are all round shaped, most probably an artifact of the tip. A maximum in phase contrast (dark) is just observed on the flank of the bacteria but not at the apical ends. In a previous section lesions on the apical ends, but not on the flank of incubated bacteria were observed. In contrast, damage at arbitrary place of the cell body was observed for the native bacteria after the drying procedure. The

correlation between the position where cell lesion is not observed and where bistability occurs, strongly supports the finding that amplitude bistability occurs due to the presence of IgA. The presence of IgA essentially helps to stabilize the shell of the bacteria.

In figure 3.8(b), topography and phase images of two flagella from IgA incubated bacteria are shown. A high phase contrast on both flagella is seen, indicating that they are fully covered with IgA. In the theory part of how *E. coli* bacteria cause infections, it has been described that the flagellum is essential to provoke infections [91, 92]. The decreased thickness of the flagellum and the fully coverage of the flagella with the IgA antibody, strongly indicate that one reason why the treatment of *E. coli* bacteria with the antibody IgA hinders them to be pathogenic is due to modification of the flagellum.

3.2.3 Summary

To conclude the chapter about the influence of IgA on the morphology changes of *E. coli* under ambient conditions. We have observed that the shape of IgA incubated bacteria upon the drying procedure is greatly preserved compared to native bacteria. Native bacteria showed lesions at arbitrary place of the cell body, whereas IgA incubated bacteria just had lesions at the apical ends. Both bacteria types showed damage of the cell body resulting in the loss of a large amount of cell liquid. The bacteria surface roughness was found to be 2 nm higher after incubation with the IgA antibody. The differences between the statistical values for the width and height of the bacteria were all in between the variance of error. Regarding the statistical values for the flagellum, a decrease in thickness after incubation with IgA was observed, indicating that the antibody somehow modified the flagellum. The high occurrence of amplitude bistability on the incubated bacteria was interpreted as a direct proof to the presence of IgA. The motion of the cantilever oscillation is perturbed due to the presence of the IgA, so that the net interaction force sensed by the tip changes from repulsive to attractive at the place where IgA is found. The high compliance of the IgA molecule results in a low contribution of the repulsive force to the total force sensed by the tip, although the tip is in intermittent contact with the sample. This results in sensing always a net attractive tip-sample force at the place where IgA is found. Such discontinuous jumps where found on the bacteria body and the flagellum.

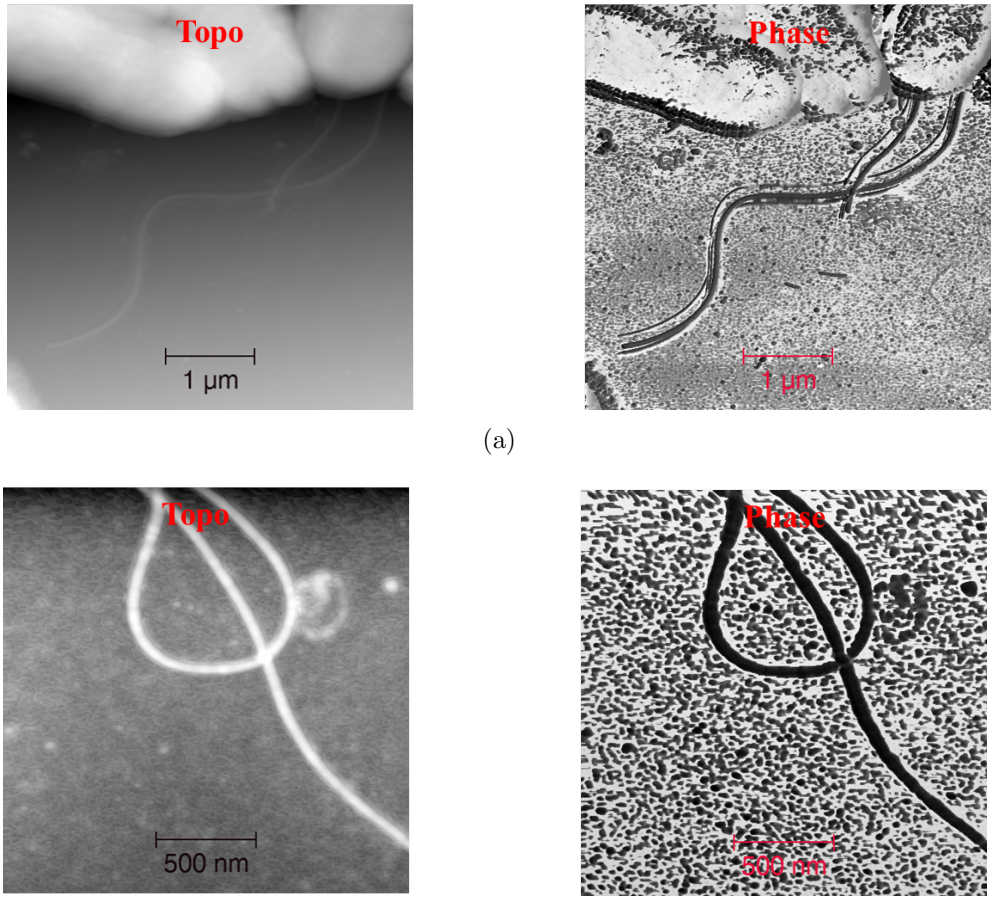

Figure 3.8: AM-AFM images taken on IgA incubated bacteria on a silicon substrate. On both images a change in phase contrast from white to dark is seen, due to amplitude bistability. In (a) discontinuous jumps in the amplitude occur on the bacteria body, the border of the bacteria and on the flagellum (darkest phase contrast). The surface covered with proteins and molecules to some extent also show bistability. (b) represents a close view of two flagella where amplitude bistability occurs. Imaging conditions: (a) $f = 183.161$ kHz, $A = 19$ nm, Set pt. $= 80$ %. (b) $f = 183.188$ kHz, $A = 13$ nm, Set pt. $= 68$ %.

3.3 Magnetic Properties of MTB

In a first part of this section, AM-AFM mode images of magnetotactic bacterium are shown where the intact magnetosome chain were made visible and their structure is discussed. In the second part, the results from cantilever magnetometry experiments of one single magnetotactic bacteria will be presented. We will discuss the intrinsic magnetic properties with respect to the magnetic moment, the anisotropy constant and the coercive field evaluated from the measurement.

Figure 3.9 shows a topography image performed in the AM-AFM imaging of chemically treated magnetic bacteria obtained under ambient imaging conditions. The red rectangles show the position of intact magnetosomes. The inset shows a zoom on one of the bacteria where an intact magnetosome chain arranged along the cell's long axis can be seen. This arrangement is the magnetically most efficient orientation of the chain within the bacteria body. The mean height of the untreated bacterias was h_{native} = 260-300 nm and after the chemical treatment a shrinking of the bacteria to a height of approximately h_{chem} = 100-140 nm was observed. This shrinking of the bacteria is due to pinning of the bacteria cell membrane and the consecutive loss of cell liquid. Due to this shrinking, it was possible to image magnetosomes in MTB in the AM-AFM mode. The reduced thickness of the bacteria enabled sensing of these structures with the tip. The treatment did not destroy the magnetosomes, as can be seen in figure 3.10(a), where a single magnetic chain is illustrated. This specific chain consists of 18 single magnets arranged in a pearl necklace fashion with an approximate length of 1μm. A line profile of a part of the chain is represented in 3.10(b). Each individual magnet is separated from the neighboring magnet by a distance of around 7-10 nm. This spacing is typical for such a magnetosome chain, as each nanomagnet is encapsulated in an individual membrane-envelope, preventing conglomeration of the magnets and enabling a certain flexibility of the chain to orient along the magnetic field. The chemical treatment somehow did destroy the outer membrane of the bacteria cell but not the membrane of the encapsulated magnetite particles inside the body of the bacteria. The dark cavities seen on the bacteria are known to be sulfur-rich and lipid storage granules, which serve the bacteria as temporary storage of compounds [128, 129].

3.3.1 Cantilever Magnetometry of Single Magnetotactic Bacterium

In figure 3.11, a f-H curve obtained from one single magnetotactic baterium is shown. The Δf signal is very low in the mHz regime, due to the small magnetic volume of one single magnetosome. The cantilever had a normal

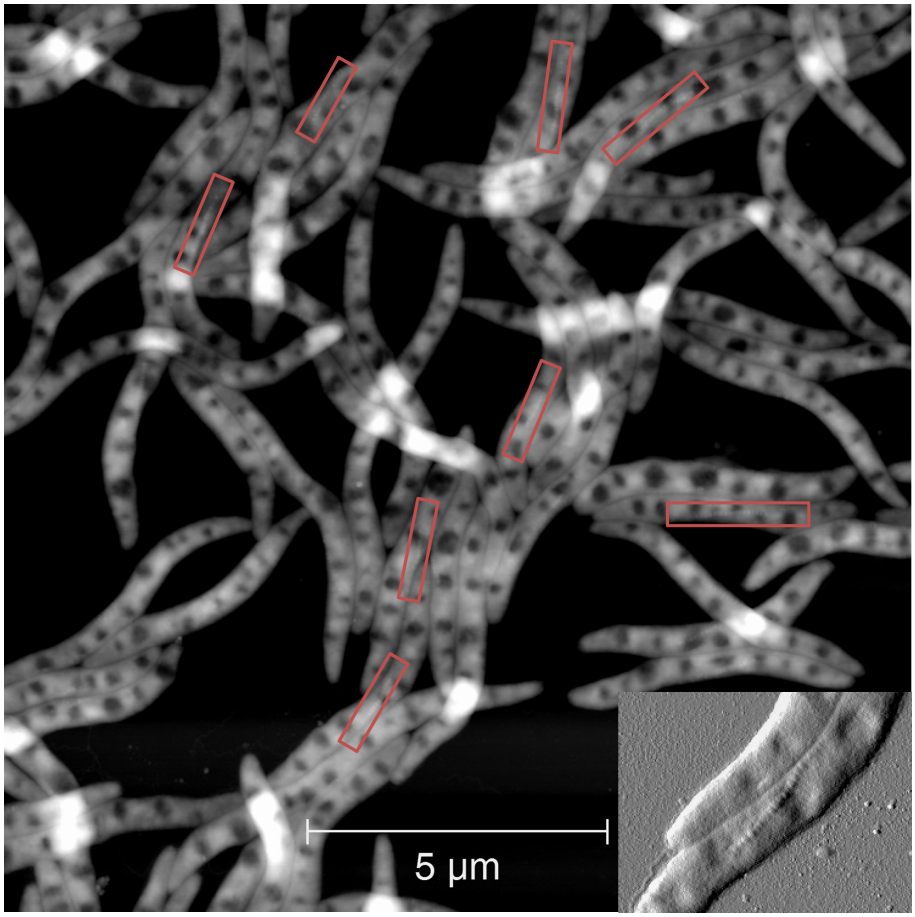

Figure 3.9: AM-AFM topography and amplitude image (inset) of the chemically treated bacteria. Some of the magnetosome chains are indicated by the red rectangles in the topography image. The amplification inset shows an amplitude image of an entire intact magnetosome chain.

spring constant of $k_N = 95\ \mu\mathrm{Nm}^{-1}$ and a quality factor of $Q = 121736$, was oscillated at a frequency $f_{res} = 2500$ Hz with a free oscillation amplitude of $A = 660$ nm. The experiment was done at a temperature of 5 K and in a variable magnetic field of $\Delta H = \pm$ 200 mT. The red and blue sweep-curves correspond to the frequency shift response of the cantilever while sweeping the magnetic field up from -200 mT to +200 mT and down from +200 mT to -200 mT, respectively. The continuous lines correspond to the fit of the experimental data with equation (1.26). The SEM images of the bacteria glued to the tip did not reveal the size and number of the magnets enclosed by the magnetosome, as the glue was covering the entire bacterium. The volume to be magnetized was estimated from the AM-AFM images obtained after chemical treatment of the bacteria, where an intact magnetosome chain, consisted of a mean number of 18 magnets

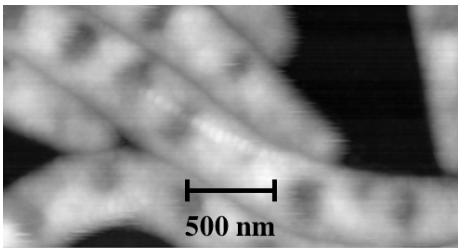

(a) Phase image of a single magnetosome chains.

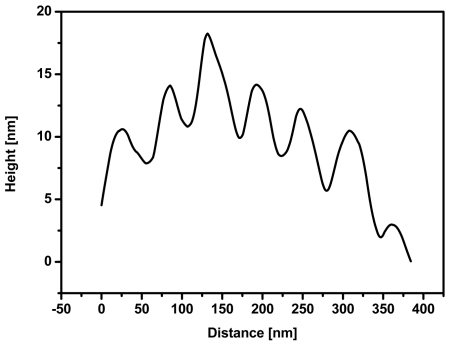

(b) Partial line scan of the magnetosome chain.

Figure 3.10: (a) AM-AFM topography image of a single magnetosome from a MTB which was chemically treated. The nanomagnets are 30-40 nm in size and are spaced one from another, indicating that the membranous structure separating them and needed to form a chain is preserved. (b) shows a line profile of a part of a magnetosome chain. One clearly sees the single magnets being spaced around 10 nm each one from another.

with a mean diameter of around 30 nm, resulting in a magnetic volume of $V = 5 \times 10^{-22}$ m^3. The parameters to fit were the magnetic moment m and the anisotropy constant K of the magnetic bacterium. The hysteresis loop enclosed between forward and backward sweep from the f-H curve is typical for a ferromagnetic systems. This hysteresis is a result of the magnetic anisotropy of ferromagnetic systems, where the samples magnetization depends on the direction of the applied magnetic field. A misalignment of the position of the magnetosome chain on the cantilever, which is rather probable, might also contribute to the hysteresis seen. The crossing of the Δf curves occurs at a magnetic field of $\mu_0 H = 0$, where the magnetization is zero. From the shape of the curve we can also conclude about the orientation of the attached magnetic sample on the cantilever. As the magnetosome chain can be regarded as a rod, the curve is typical for a rod which is placed in an orientation along the cantilever axis [130]. The system was magnetically saturated at a magnetic field of $\mu_0 H = 120$ mT.

The derived equation for a ferromagnetic rod to fit the data, highly correlates with the experimental data. The model from Stoner and Wohlfarth for ferromagnetic single domain particles, with uniform magnetization, shows to be suitable to simulate the magnetic response of one single magnetotactic bacterium. The fitting agrees well with the experimental data up to a magnetic field of $\mu_0 H = \pm 150$ mT, beyond this point the experimental and the fitted curves start to differ. At this point the experimental frequency shift response decreases and starts to oscillate, while the simulated

frequency shift increase with increasing the external magnetic field. The origin of this behavior is not clearly understood. One reason could be, that the magnets in the magnetosome chains start to align along the external applied magnetic field lines, reducing the magnetization and hence the torque of the cantilever resulting in a decrease of the frequency shift response of the cantilever. In case of a parallel alignment of the magnetization vector $\vec{M}$ with the magnetic field vector $\vec{H}_{ext}$, the torque τ of the cantilever is zero which is easily understood by having a look at this fundamental relationship of how cantilever magnetometry works $\tau{=}\mu_0 V(\vec{M}{\times}\vec{H}_{ext})$. This would indicate that the magnetic field is strong enough to move the magnets in the magnetosome chain within the bacteria even at a temperature of 5 K.

3.3.2 Magnetic Moment and Anisotropy Constant of Single Magnetotactic Bacterium

A magnetic moment of the chain of $m = 5.2 \times 10^{-16}$ A m^2 was obtained from fitting the experimental data. This value is in very good agreement with the values found in the literature. In table 3.4 an overview of the experimentally determined magnetic moment value of magnetotactic bacteria reported in the literature is shown. Different methods were applied on distinct magnetic bacteria species, where only Dunnin *et. al* [62] analyzed the magnetic properties of one single bacterium. In other cases the experimentally determined values were obtained from averaging over multiple bacteria. Cantilever magnetometry opens the possibility to not only explore the magnetic moment of objects, but also determine the anisotropy constant.

The anisotropy constant derived from fitting the experimental data takes into account all kind of directional dependent magnetic anisotropies of the magnetosome chain. An effective magnetic anisotropy constant of $K_{eff} = 5 \times 10^4$ J m^{-3} was obtained from fitting. This effective anisotropy constant K_{eff} is found to be 3.7-times higher than the first-order magneto-crystalline anisotropy constant for bulk magnetite $K_1^{bulk} = 1.35 \times 10^4$ J m^{-3} [62]. For bulk systems the anisotropy strongly depends on the crystal structure of the system, where the first order magneto-crystalline constant K_1 rises from spin-orbit interaction between the orbital motion of the electrons that couple to the crystal electric field. An increase of the anisotropy constant for an ensemble of nanometer sized particles compared to bulk has been reported in another study [131]. This increase of the energy barrier for particle ensembles, like in a magnetosome, can strongly be affected by the interparticle interaction, where the contributions of neighboring magnetic dipole moments can be so large that they are stronger than the particle specific crystalline or shape anisotropy. Another study concluded the same finding

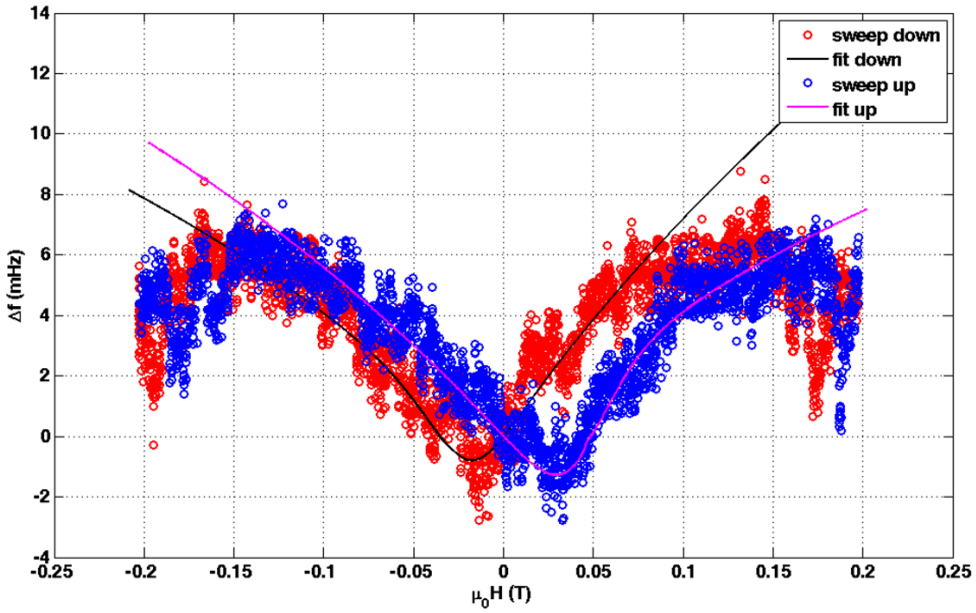

Figure 3.11: Cantilever magnetometry f-H curve obtained for one single magnetotactic bacterium for a magnetic field of $\Delta\mu_0 H = \pm$ 200 mT, f_{res} = 2500 Hz, A = 660 nm, Q = 121736 and a temperature of 5 K. The red and blue curve correspond to the experimental data while sweeping the magnetic field down and up, respectively. The continuous lines were obtained while fitting the experimental data with equation (1.26).

using a different measuring technique, where they showed that dipolar interactions of the magnets in the magnetosome chains dictate the magnetic anisotropy [132].

3.3.3 Coercive Field and Discrete Δf Steps

From figure 3.11, a coercive field of H_c = 40 mT can be read out. The coercive field is a specific material property of ferromagnetic or ferroelectric materials to withstand an external magnetic or electric magnetic field. In case of a ferromagnetic material it indicates at which magnetic field the magnetization drop to zero for a system having previously reached saturation. A mean coercive field value of H_c = 30-50 mT was reported for single domain magnetite ensembles present in sockeye salmon [135] and yellow-fin tuna [136]. Such coercive field values are typical for biogenically produced magnetic crystals in presence of interacting single domain magnetite [137]. The coercive field value of 40 mT obtained from the cantilever magnetometry measurement of a single magnetotactic bacterium is in very good agreement with the value found in the literature. The interaction of these single domain magnetite in the magnetosome chain dominates the magnetic

Table 3.4: Method and measured magnetic moment μ of MTB reported in the literature

Method	MTB species	Measured μ (A $\times$ m^2)	Author
Cantilever magnetometry (single bacterium)	*M. gryphenwaldense*	4.5×10^{-16}	**Our results**
Electron Holography (single bacterium)	*M. magnetotacticum*	5×10^{-16}	Dunnin *et. al* [62]
Cantilever magnetometry (over 100 species simultaneously)	*M. gryphenwaldense*	5×10^{-16}	Gysin *et. al* [61]
Wide-field magnetic imaging microscope (statistically over many bacteria)	*M. magnetotacticum*	0.5×10^{-16}	Le Sage *et. al* [133]
Comparing different methods (statistically over many bacteria)	*M. magnetotacticum*	1-7.1 $\times 10^{-16}$	Nadkarin *et. al* [134]

properties of the whole chain, which was also concluded in the previous section about the discussion of the effective anisotropy constant value.
In figure 3.12, a f-H curve is shown where discrete steps in the Δf signal are observed. The black circles on this figure show two specific Δf plateaus at magnetic fields of $\mu_0 H = 30$ mT and 60 mT. The solid lines in this figure are just illustrated to guide the eye and were obtained by simply fitting the experimental data with a polynomial. Multiple plateaus in the Δf signal are observed. Certainly the data is noisy but nonetheless discontinuous jumps in the frequency shift response of the cantilever are found, which we believe are not an artefact of the noise. Such discrete Δf steps have been observed in the literature for individual 6 μm long and 140 nm wide ferromagnetic Ni nanotubes with dynamic cantilever magnetometry and were attributed to abrupt changes in the volume magnetization due to switching of discrete magnetic domains [138]. In this experiment such an event resulted in a jump of the Δf signal of approximately 500 mHz, appearing on both branches at the same magnetic field for sweeping the magnetic field up and down. In our case the discrete switching of the Δf signal is in the mHz regime and does not appear precisely at the same magnetic field on both branches. The small Δf signal is due to the fact that the individual single domain magnets in the magnetosome, which have a diameter of around 30 nm, cause a low change in the volume magnetization upon reversal. For example, the specific discontinuous jumps in the Δf signal illustrated with black circles in figure 3.12 are in the order of 2 mHz. Possible explanation why switching is not observed symmetrically on both branches is misalignment of the magnetosome chain, where the hard- and easy axis of the magnets are not precisely within the oscillation plane of the cantilever.

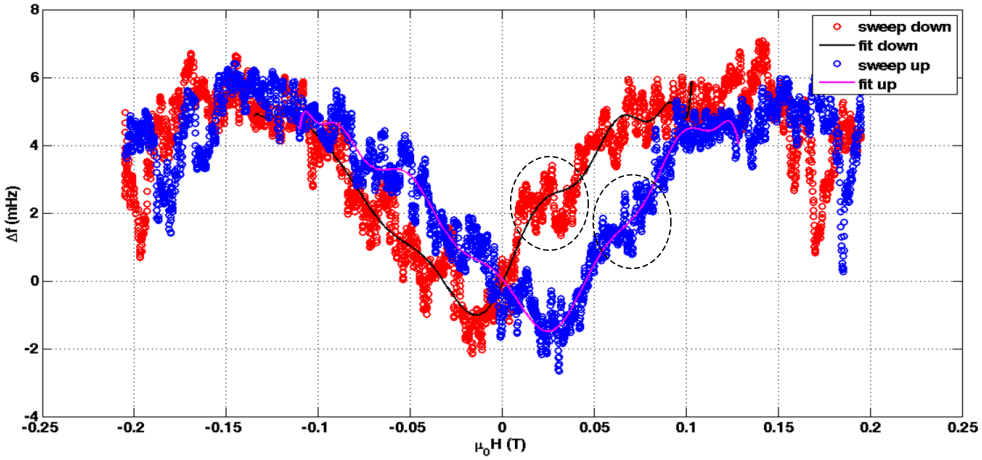

Figure 3.12: A f vs H curve of a cantilever with one single magnetotactic bacterium attached at the free end of it, obtained for a magnetic field of $\Delta\mu_0 H = 200$ mT and a temperature of 5 K. The solid lines correspond to a curve fitting over a polynomial and are just illustrated to guide the eye. The dashed circles indicate two positions where presumably discrete switching of single magnetosomes occur.

3.3.4 Summary

To conclude this chapter. In a first part, we examined the magnetosome of one single magnetotactic bacterium with AM-AFM under ambient measurement conditions. We showed that the nanomagnets in the chain have a mean diameter of 30 nm and are equally separated from one another with a distance of around 10 nm. Each nanomagnet is encapsulated in a membrane forming a chain of single domain particles. Cantilever magnetometry measurements enabled to record a f-H curve where a hysteresis between forward and backward curve is drawn, which is typical for a ferromagnetic material. The shape of the curve also showed that the magnetosome chains was aligned in an orientation along the cantilever axis. The curve was then successfully fitted with the formula of a ferromagnetic rod, where the single bacterium revealed a magnetic moment of the bacterium of $m = 5.2 \times 10^{-16}$ A m^2 which is in good agreement with literature values found. The Stoner and Wohlfarth model showed to be suitable to describe the magnetization of one single magnetotactic bacterium. Furthermore an anisotropy constant of $K_{eff} = 5 \times 10^4$ J m^{-3} and a coercive field of $H_c = 40$ mT were extracted from the experimental data, which are typical for single domain biogenically produced ferromagnetic particles, where the magnetic properties are predominantly dominated by the interaction energy between these particles. We also observed single Δf steps which we attribute to a reversal of the magnetization within single domain in the magnetosome chain.

Chapter 4

Conclusions and Outlook

In the first part of the work, we compared the retention properties of synthesized CaF_2 nanoparticles adsorbed on mica and on polished tooth enamel in liquid. From the phase-lag of the cantilever with respect to the excitation signal we calculated the power dissipation at the point the nanoparticles were mobilized. By comparing the frequency distribution of the obtained dissipated power, we showed that up to 10-times higher retention was observed for particles adsorbed on tooth enamel compared to mica. Although the enamel had an increased surface roughness compared to mica resulting in a decreased contact area of the particle with the substrate, more power was needed to dislocate the particles. We relate this to the strong chemical interaction of the CaF_2 nanoparticles with the tooth enamel. Further, we have shown that particles with an ordered, smooth and plane surface structure show higher retention than rough and spherical ones. Thus, the nano-morphology of particles has a strong influence on the mobility. The evidence that the interplay of calcium fluoride nanoparticles with the tooth enamel is so strong, makes calcium fluoride nanoparticles in respect to their adhesive strength on tooth enamel a promising candidate to be used in dental care products preventing teeth demineralization. Further solubility tests need to be done in order to examine their acid dependent fluoride release over time. We showed that AM-AFM is a powerful tool to compare detachment and interaction properties of adsorbates in liquid.

In the second part, we examined the effect of antibody IgA on the change of morphology on *E. coli* bacteria. Images of native and incubated bacteria revealed a much higher stability of the incubated bacteria against the drying procedure as part of the sample preparation. Less lesions of the bacteria body and a much more homogeneous body structure after treatment with the antibody were observed. The incubated bacteria also showed a higher degree in surface roughness after incubation, a clear indication that the antibody covers the bacteria body. The statistically evaluated values for the

width and the height of the entire bacteria and the flagellum have revealed a slightly lower thickness of the flagella. An indication where the antibody IgA exactly binds to the bacterium was obtained from AM-AFM images, where a high tendency of amplitude to show bistability was observed. Each bistability event was interpreted as a result of the presence of the antibody. A high tendency of the amplitude to show bistable behaviour was seen on the bacteria body and on the whole flagella for IgA incubated bacteria. We showed that the IgA binds to the bacteria body and the flagellum, where the modification of the flagellum strongly could influence the mobility and hence the possibility of pathogenic *E. coli* bacteria to enter into blood circulated tissues to cause infections. Further experiment under liquid conditions are needed, where living bacteria could be examined without lesions coming from the drying procedure. Experiments with a high speed AFM in liquid would enable to examine *in situ* the influence of IgA after injection to pathogenic *E. coli* bacteria.

The third part of the thesis, examined the magnetic properties of an single magnetotactic bacterium. We were able to position one single bacterium at the free end of sensitive tip-less cantilever with the help of a micro mechanical manipulator. The dynamic cantilever magnetometry measurements were performed under UHV conditions at 5 K. The data showed excellent agreement with the theoretical model. The shape of the f-H curve was typical for a ferromagnetic material which is placed on the cantilever in a orientation parallel to the cantilever axis. The magnetic moment of a single magnetosome chain fitted with the derived equation of a ferromagnetic rod, gave a value of $m = 5.2 \times 10^{-16}$ A m^2. This value is in very good agreement with the values found in the literature. Compared to other studies, the cantilever magnetometry method allowed us to not only to determine the magnetic moment of a single magnetic bacteria, but also provided information about anisotropy constant or the coercive field of a single magentosome chain. An effective anisotropy constant of $K_{eff} = 5 \times 10^4$ J m^{-3} was obtained from the fit to the experimental data. This anisotropy constant was found to be higher than the first order magnetocrystalline constant for bulk magnetite. The higher anisotropy constant was consistent with other studies, showing that for an ensemble of nano-sized magnets the interparticle interaction is stronger than the intrinsic magnetic anisotropy behaviour of single domain particles. A coercive field of $H_c = 40$ mT was measured with cantilever magnetometry, which is in very good agreement with other values reported in the literature of biogenic produced magnetite crystals. A coercive field value between $H_c = 30$-50 mT is typical for interacting single domain magnetite in biological tissues. From the value of the anisotropy constant K_{eff} and the coercive field H_c we concluded that the magnetic interaction between

the single magnetite crystals dictate the magnetic properties of the magnetosome chain. Discrete Δf steps in the f-H experiment were attributed to a change of the volume magnetization due to switching of magnetic single domains. Further experiments with even more sensitive cantilevers might enable to examine more precisely the single switching behavior of domains in the magnetosome chain.

Bibliography

[1] C.M. Mate, G. McClelland, R. Erlandsson, and S. Chiang. Atomic-scale friction of a tungsten tip on a graphite surface. *Physical Review Letters*, 59(17):1942–1945, October 1987.

[2] L. Gross, F. Mohn, N. Moll, P. Liljeroth, and G. Meyer. The chemical structure of a molecule resolved by atomic force microscopy. *Science*, 325(5944):1110–1114, August 2009.

[3] S. Rozhok, P. Sun, R. Piner, M. Lieberman, and C.A. Mirkin. AFM Study of Water Meniscus Formation between an AFM Tip and NaCl Substrate. *The Journal of Physical Chemistry B*, 108(23):7814–7819, June 2004.

[4] D. Sarid. *Scanning Force Microscopy*. Oxford University Press, 1991.

[5] F.J. Giessibl. Atomic resolution on Si(111)-(7x7) by noncontact atomic force microscopy with a force sensor based on a quartz tuning fork. *Applied Physics Letters*, 76(11):1470, 2000.

[6] J. Tamayo and R. García. Deformation, Contact Time, and Phase Contrast in Tapping Mode Scanning Force Microscopy. *Langmuir*, 12(18):4430–4435, January 1996.

[7] N.A. Burnham, O.P. Behrend, F. Oulevey, G. Gremaud, P.-J. Gallo, D. Gourdon, E. Dupas, A.J. Kulik, H.M. Pollock, and G.A.D. Briggs. How does a tip tap? *Nanotechnology*, 8(2):67–75, June 1997.

[8] Á. Paulo and R. García. Tip-surface forces, amplitude, and energy dissipation in amplitude-modulation (tapping mode) force microscopy. *Physical Review B*, 64(19), October 2001.

[9] K.L. Johnson, K. Kendall, and A.D. Roberts. Surface Energy and the Contact of Elastic Solids. *Proceedings of the Royal Society A: Mathematical, Physical and Engineering Sciences*, 324(1558):301–313, September 1971.

[10] B.V. Derjaguin, V.M. Muller, and Y.P. Toporov. Effect of contact deformations on the adhesion of particles. *Journal of Colloid and Interface Science*, 53(2):314–326, November 1975.

[11] J. Tamayo and R. García. Deformation, Contact Time, and Phase Contrast in Tapping Mode Scanning Force Microscopy. *Langmuir*, 12(18):4430–4435, January 1996.

[12] S.N. Magonov, V. Elings, and M.-H. Whangbo. Phase imaging and stiffness in tapping-mode atomic force microscopy. *Surface Science*, 375(2-3):385–391, April 1997.

[13] J.P. Cleveland, B. Anczykowski, A.E. Schmid, and V.B. Elings. Energy dissipation in tapping-mode atomic force microscopy. *Applied Physics Letters*, 72(20):2613, 1998.

[14] B. Anczykowski, B. Gotsmann, H. Fuchs, J.P. Cleveland, and V.B. Elings. How to measure energy dissipation in dynamic mode atomic force microscopy. *Applied Surface Science*, 140(3-4):376–382, February 1999.

[15] J. Tamayo and R. García. Relationship between phase shift and energy dissipation in tapping-mode scanning force microscopy. *Applied Physics Letters*, 73(20):2926, 1998.

[16] P.K. Hansma, J.P. Cleveland, M. Radmacher, D.A. Walters, P.E. Hillner, M. Bezanilla, M. Fritz, D. Vie, H.G. Hansma, C.B. Prater, J. Massie, L. Fukunaga, J. Gurley, and V. Elings. Tapping mode atomic force microscopy in liquids. *Applied Physics Letters*, 64(13):1738, 1994.

[17] C.A.J. Putman, K.O. Van der Werf, B.G. De Grooth, N.F. Van Hulst, and J. Greve. Tapping mode atomic force microscopy in liquid. *Applied Physics Letters*, 64(18):2454, 1994.

[18] J. Melcher, C. Carrasco, X. Xu, J.L. Carrascosa, J. Gómez-Herrero, P. José de Pablo, and A. Raman. Origins of phase contrast in the atomic force microscope in liquids. *Proceedings of the National Academy of Sciences of the United States of America*, 106(33):13655–60, August 2009.

[19] A.F. Payam, J.R. Ramos, and R. García. Molecular and nanoscale compositional contrast of soft matter in liquid: interplay between elastic and dissipative interactions. *ACS Nano*, 6(6):4663–4670, June 2012.

[20] U. Rabe, K. Janser, and W. Arnold. Vibrations of free and surface-coupled atomic force microscope cantilevers: Theory and experiment. *Review of Scientific Instruments*, 67(9):3281, 1996.

[21] P. Maivald, H.J. Butt, S.A.C. Gould, C.B. Prater, B. Drake, J.A. Gurley, V.B. Elings, and P.K. Hansma. Using force modulation to image surface elasticities with the atomic force microscope. *Nanotechnology*, 2(2):103–106, April 1991.

[22] K. Yamanaka and S. Nakano. Quantitative elasticity evaluation by contact resonance in an atomic force microscope. *Applied Physics A: Materials Science & Processing*, 66(7):S313–S317, March 1998.

[23] E. Meyer. Atomic force microscopy. *Progress in Surface Science*, 41(1):3–49, September 1992.

[24] S. Hudlet, M. Saint Jean, C. Guthmann, and J. Berger. Evaluation of the capacitive force between an atomic force microscopy tip and a metallic surface. *The European Physical Journal B*, 2(1):5–10, April 1998.

[25] B. Bhushan. Adhesion and stiction: Mechanisms, measurement techniques, and methods for reduction. *Journal of Vacuum Science & Technology B: Microelectronics and Nanometer Structures*, 21(6):2262, 2003.

[26] A. Paiva, N. Sheller, M.D. Foster, A.J. Crosby, and K.R. Shull. Study of the Surface Adhesion of Pressure-Sensitive Adhesives by Atomic Force Microscopy and Spherical Indenter Tests. *Macromolecules*, 33(5):1878–1881, March 2000.

[27] S. Joo and D.F. Baldwin. Adhesion mechanisms of nanoparticle silver to substrate materials: identification. *Nanotechnology*, 21(5):055204, February 2010.

[28] A.J. Kinloch. Interfacial Fracture Mechanical Aspects of Adhesive Bonded Joints - A Review. *The Journal of Adhesion*, 10(3):193–219, January 1979.

[29] B. Bhushan. *Springer Handbook of Nanotechnology*. Springer Berlin Heidelberg, 2nd edition, 2007.

[30] C.A. Otter, P.J. Patty, M.A.K. Williams, M.R. Waterland, and S.G. Telfer. Mechanically interlocked gold and silver nanoparticles using metallosupramolecular catenane chemistry. *Nanoscale*, 3(3):941–944, March 2011.

[31] A.N. Gent and C.-W. Lin. Model Studies of the Effect of Surface Roughness and Mechanical Interlocking on Adhesion. *The Journal of Adhesion*, 32(2):113–125, August 1990.

[32] J. Tien, A. Terfort, and G.M. Whitesides. Microfabrication through Electrostatic Self-Assembly. *Langmuir*, 13(20):5349–5355, October 1997.

[33] Y.-L. Ong, A. Razatos, G. Georgiou, and M.M. Sharma. Adhesion Forces between E. coli Bacteria and Biomaterial Surfaces. *Langmuir*, 15(8):2719–2725, April 1999.

[34] F. Awaja, M. Gilbert, G. Kelly, B. Fox, and P.J. Pigram. Adhesion of polymers. *Progress in Polymer Science*, 34(9):948–968, September 2009.

[35] B.V. Derjaguin, I.N. Aleinikova, and Y.P. Toporov. On the role of electrostatic forces in the adhesion of polymer particles to solid surfaces. *Powder Technology*, 2(3):154–158, March 1969.

[36] D.M. Eigler and E.K. Schweizer. Positioning single atoms with a scanning tunnelling microscope. *Nature*, 344(6266):524–526, April 1990.

[37] C. Baur, A. Bugacov, B.E. Koel, A. Madhukar, N. Montoya, T.R. Ramachandran, A.A.G. Requicha, R. Resch, and P. Will. Nanoparticle manipulation by mechanical pushing: underlying phenomena and real-time monitoring. *Nanotechnology*, 9(4):360–364, December 1998.

[38] D. Dietzel, T. Mönninghoff, L. Jansen, H. Fuchs, C. Ritter, U.D. Schwarz, and A. Schirmeisen. Interfacial friction obtained by lateral manipulation of nanoparticles using atomic force microscopy techniques. *Journal of Applied Physics*, 102(8):084306, 2007.

[39] D. Dietzel, T. Mönninghoff, C. Herding, M. Feldmann, H. Fuchs, B. Stegemann, C. Ritter, U. Schwarz, and A. Schirmeisen. Frictional duality of metallic nanoparticles: Influence of particle morphology, orientation, and air exposure. *Physical Review B*, 82(3), July 2010.

[40] M. Palacio and B. Bhushan. A nanoscale friction investigation during the manipulation of nanoparticles in controlled environments. *Nanotechnology*, 19(31):315710, August 2008.

[41] D. Dietzel, M. Feldmann, C. Herding, U.D. Schwarz, and A. Schirmeisen. Quantifying Pathways and Friction of Nanoparticles During Controlled Manipulation by Contact-Mode Atomic Force Microscopy. *Tribology Letters*, 39(3):273–281, June 2010.

[42] R. Lüthi, E. Meyer, H. Haefke, L. Howald, W. Gutmannsbauer, and H.-J. Güntherodt. Sled-type motion on the nanometer scale: determination of dissipation and cohesive energies of c60. *Science*, 266(5193):1979–81, December 1994.

[43] M. Sitti and H. Hashimoto. Controlled pushing of nanoparticles: modeling and experiments. *IEEE/ASME Transactions on Mechatronics*, 5(2):199–211, June 2000.

[44] C. Ritter, M. Heyde, B. Stegemann, K. Rademann, and U. Schwarz. Contact-area dependence of frictional forces: Moving adsorbed antimony nanoparticles. *Physical Review B*, 71(8):085405, February 2005.

[45] G. Paolicelli, M. Rovatti, A. Vanossi, and S. Valeri. Controlling single cluster dynamics at the nanoscale. *Applied Physics Letters*, 95(14):143121, 2009.

[46] K. Mougin, E. Gnecco, A. Rao, M.T. Cuberes, S. Jayaraman, E.W. McFarland, H. Haidara, and E. Meyer. Manipulation of gold nanoparticles: influence of surface chemistry, temperature, and environment (vacuum versus ambient atmosphere). *Langmuir*, 24(4):1577–1581, February 2008.

[47] S. Darwich, K. Mougin, A. Rao, E. Gnecco, S. Jayaraman, and H. Haidara. Manipulation of gold colloidal nanoparticles with atomic force microscopy in dynamic mode: influence of particle - substrate chemistry and morphology, and of operating conditions. *Beilstein Journal of Nanotechnology*, 2:85–98, February 2011.

[48] A. Rao, E. Gnecco, D. Marchetto, K. Mougin, M. Schönenberger, S. Valeri, and E. Meyer. The analytical relations between particles and probe trajectories in atomic force microscope nanomanipulation. *Nanotechnology*, 20(11):115706, March 2009.

[49] A. San Paulo and R. García. High-resolution imaging of antibodies by tapping-mode atomic force microscopy: attractive and repulsive tip-sample interaction regimes. *Biophysical Journal*, 78(3):1599–1605, March 2000.

[50] R.W. Stark. Bistability, higher harmonics, and chaos in AFM. *Materials Today*, 13(9):24–32, September 2010.

[51] R. García and A. San Paulo. Dynamics of a vibrating tip near or in intermittent contact with a surface. *Physical Review B*, 61(20):13381–13384, May 2000.

[52] R. García and A. San Paulo. Attractive and repulsive tip-sample interaction regimes in tapping-mode atomic force microscopy. *Physical Review B*, 60(7):4961–4967, August 1999.

[53] R. García and R. Pérez. Dynamic atomic force microscopy methods. *Surface Science Reports*, 47(6-8):197–301, September 2002.

[54] D. Rugar, H.J. Mamin, P. Guethner, S.E. Lambert, J.E. Stern, I. McFadyen, and T. Yogi. Magnetic force microscopy: General principles and application to longitudinal recording media. *Journal of Applied Physics*, 68(3):1169, 1990.

[55] U. Hartmann. Magnetic Force Microscopy. *Annual Review of Materials Science*, 29(1):53–87, August 1999.

[56] C. Lupien, B. Ellman, P. Grütter, and L. Taillefer. Piezoresistive torque magnetometry below 1 K. *Applied Physics Letters*, 74(3):451, 1999.

[57] E.C. Stoner and E.P. Wohlfarth. A Mechanism of Magnetic Hysteresis in Heterogeneous Alloys. *Philosophical Transactions of the Royal Society A: Mathematical, Physical and Engineering Sciences*, 240(826):599–642, May 1948.

[58] L.D. Landau, J.S. Bell, M.J. Kearsley, L.P. Pitaevskii, E.M. Lifshitz, and J.B. Sykes. *Electrodynamics of continuous media*, volume 8. Elsevier, 1984.

[59] J. Sidles, J. Garbini, K. Bruland, D. Rugar, O. Züger, S. Hoen, and C. Yannoni. Magnetic resonance force microscopy. *Reviews of Modern Physics*, 67(1):249–265, January 1995.

[60] B. Stipe, H. Mamin, T. Stowe, T. Kenny, and D. Rugar. Magnetic Dissipation and Fluctuations in Individual Nanomagnets Measured by Ultrasensitive Cantilever Magnetometry. *Physical Review Letters*, 86(13):2874–2877, March 2001.

[61] U. Gysin, S. Rast, A. Aste, T. Speliotis, C. Werle, and E. Meyer. Magnetic properties of nanomagnetic and biomagnetic systems analyzed using cantilever magnetometry. *Nanotechnology*, 22(28):285715, July 2011.

[62] R.E. Dunin-Borkowski. Magnetic Microstructure of Magnetotactic Bacteria by Electron Holography. *Science*, 282(5395):1868–1870, December 1998.

[63] T.R. Albrecht, P. Grütter, D. Horne, and D. Rugar. Frequency modulation detection using high-Q cantilevers for enhanced force microscope sensitivity. *Journal of Applied Physics*, 69(2):668, 1991.

[64] S. Rast, U. Gysin, and E. Meyer. Phase noise induced due to amplitude fluctuations in dynamic force microscopy. *Physical Review B*, 79(5):054106, February 2009.

[65] C. Feldmann, M. Roming, and K. Trampert. Polyol-mediated synthesis of nanoscale CaF2 and CaF2:Ce,Tb. *Small*, 2(11):1248–1250, November 2006.

[66] L. Wang, B. Wang, X. Wang, and W. Liu. Tribological investigation of CaF2 nanocrystals as grease additives. *Tribology International*, 40(7):1179–1185, July 2007.

[67] H.H.K. Xu, J.L. Moreau, L. Sun, and L.C. Chow. Novel CaF(2) nanocomposite with high strength and fluoride ion release. *Journal of Dental Research*, 89(7):739–745, 2010.

[68] H.H.K. Xu, M.D. Weir, L. Sun, J.L. Moreau, S. Takagi, L.C. Chow, and J.M. Antonucci. Strong nanocomposites with Ca, PO(4), and F release for caries inhibition. *Journal of Dental Research*, 89(1):19–28, January 2010.

[69] M. Azami, S. Jalilifiroozinezhad, M. Mozafari, and M. Rabiee. Synthesis and solubility of calcium fluoride/hydroxy-fluorapatite nanocrystals for dental applications. *Ceramics International*, 37(6):2007–2014, August 2011.

[70] M.J. Larsen and S.J. Jensen. Experiments on the initiation of calcium fluoride formation with reference to the solubility of dental enamel and brushite. *Archives of oral biology*, 39(1):23–27, January 1994.

[71] F. Lippert, D.M. Parker, and K.D. Jandt. In vitro demineralization/remineralization cycles at human tooth enamel surfaces investigated by AFM and nanoindentation. *Journal of Colloid and Interface Science*, 280(2):442–448, December 2004.

[72] S.E. Cross, J. Kreth, R.P. Wali, Ri. Sullivan, W. Shi, and J.K. Gimzewski. Evaluation of bacteria-induced enamel demineralization using optical profilometry. *Dental Materials*, 25(12):1517–1526, December 2009.

[73] I.M. Pelin, A. Piednoir, D. Machon, P. Farge, C. Pirat, and S.M.M. Ramos. Adhesion forces between AFM tips and superficial dentin

surfaces. *Journal of Colloid and Interface Science*, 376(1):262–268, June 2012.

[74] A. Lussi, T. Jaeggi, C. Gerber, and B. Megert. Effect of amine/sodium fluoride rinsing on toothbrush abrasion of softened enamel in situ. *Caries Research*, 38(6):567–571, 2004.

[75] J.L. Moreau and H.H.K. Xu. Fluoride releasing restorative materials: Effects of pH on mechanical properties and ion release. *Dental Materials*, 26(11):227–235, November 2010.

[76] M. Petzold. The Influence of Different Fluoride Compounds and Treatment Conditions on Dental Enamel: A Descriptive in vitro Study of the CaF2 Precipitation and Microstructure. *Caries Research*, 35:45–51, January 2001.

[77] H.-B. Pan and B.W. Darvell. Solubility of calcium fluoride and fluorapatite by solid titration. *Archives of Oral Biology*, 52(9):861–868, September 2007.

[78] J.A. Dirksen and T.A. Ring. Fundamentals of crystallization: Kinetic effects on particle size distributions and morphology. *Chemical Engineering Science*, 46(10):2389–2427, January 1991.

[79] C. Burda, X. Chen, R. Narayanan, and M.A. El-Sayed. Chemistry and properties of nanocrystals of different shapes. *Chemical Reviews*, 105(4):1025–1102, April 2005.

[80] J.-F. Chen, Y.-H. Wang, F. Guo, X.-M. Wang, and C. Zheng. Synthesis of Nanoparticles with Novel Technology: High-Gravity Reactive Precipitation. *Industrial & Engineering Chemistry Research*, 39(4):948–954, April 2000.

[81] V. Uskoković and L.E. Bertassoni. Nanotechnology in Dental Sciences: Moving towards a Finer Way of Doing Dentistry. *Materials*, 3(3):1674–1691, March 2010.

[82] T.M. Smith, A.J. Olejniczak, D.J. Reid, R.J. Ferrell, and J.J. Hublin. Modern human molar enamel thickness and enamel-dentine junction shape. *Archives of Oral Biology*, 51(11):974–995, November 2006.

[83] R.L. Guerrant, T.S. Steiner, A.A. Lima, and D.A. Bobak. How intestinal bacteria cause disease. *The Journal of Infectious Diseases*, 179:331–337, March 1999.

[84] V.T. Lee and O. Schneewind. Protein secretion and the pathogenesis of bacterial infections. *Genes & Development*, 15(14):1725–1752, July 2001.

[85] M.E. Lamm. Interaction of antigens and antibodies at mucosal surfaces. *Annual Review of Microbiology*, 51:311–340, January 1997.

[86] M.A. Kerr. The structure and function of human IgA. *The Biochemical Journal*, 271(2):285–296, 1990.

[87] J. Mestecky, M.W. Russell, and C.O. Elson. Intestinal IgA: novel views on its function in the defence of the largest mucosal surface. *Gut*, 44(1):2–5, January 1999.

[88] N.J. Mantis, N. Rol, and B. Corthésy. Secretory IgA's complex roles in immunity and mucosal homeostasis in the gut. *Mucosal Immunology*, 4(6):603–611, November 2011.

[89] R.C. Williams and R.J. Gibbons. Inhibition of Bacterial Adherence by Secretory Immunoglobulin A: A Mechanism of Antigen Disposal. *Science*, 177(4050):697–699, August 1972.

[90] J.B. Kaper, J.P. Nataro, and H.L. Mobley. Pathogenic Escherichia coli. *Nature Reviews Microbiology*, 2(2):123–140, February 2004.

[91] C. Pichon, C. Héchard, L. du Merle, C. Chaudray, I. Bonne, S. Guadagnini, A. Vandewalle, and C. Le Bouguénec. Uropathogenic Escherichia coli AL511 requires flagellum to enter renal collecting duct cells. *Cellular Microbiology*, 11(4):616–628, April 2009.

[92] W.R. Schwan. Flagella allow uropathogenic Escherichia coli ascension into murine kidneys. *International Journal of Medical Microbiology*, 298(5-6):441–447, July 2008.

[93] H.C. Berg. The rotary motor of bacterial flagella. *Annual Review of Biochemistry*, 72:19–54, January 2003.

[94] R. Blakemore. Magnetotactic bacteria. *Science*, 190(4212):377–379, October 1975.

[95] D. Faivre and D. Schüler. Magnetotactic bacteria and magnetosomes. *Chemical Reviews*, 108(11):4875–4898, November 2008.

[96] R.B. Frankel, D.A. Bazylinski, M.S. Johnson, and B.L. Taylor. Magneto-aerotaxis in marine coccoid bacteria. *Biophysical Journal*, 73(2):994–1000, August 1997.

[97] R. Wiltschko and W. Wiltschko. Magnetotaxis and Alignment Behaviors. In *Magnetic Orientation in Animals*, pages 27–41. Springer Berlin Heidelberg, 1995.

[98] N. Krumov, I. Perner-Nochta, S. Oder, V. Gotcheva, A. Angelov, and C. Posten. Production of Inorganic Nanoparticles by Microorganisms. *Chemical Engineering & Technology*, 32(7):1026–1035, July 2009.

[99] A. Scheffel, M. Gruska, D. Faivre, A. Linaroudis, J.M. Plitzko, and D. Schüler. An acidic protein aligns magnetosomes along a filamentous structure in magnetotactic bacteria. *Nature*, 440(7080):110–114, March 2006.

[100] J. Baumgartner and D. Faivre. Magnetite biomineralization in bacteria. In W.E.G. Müller, editor, *Molecular Biomineralization: Progress in Molecular and Subcellular Biology*, volume 52, pages 3–27. Springer Berlin Heidelberg, January 2011.

[101] M. Albrecht, V. Janke, S. Sievers, U. Siegner, D. Schüler, and U. Heyen. Scanning force microspy study of biogenic nanoparticles for medical applications. *Journal of Magnetism and Magnetic Materials*, 290-291:269–271, April 2005.

[102] M.R. Benoit, D. Mayer, Y. Barak, I.Y. Chen, W. Hu, Z. Cheng, S.X. Wang, D.M. Spielman, S.S. Gambhir, and A. Matin. Visualizing implanted tumors in mice with magnetic resonance imaging using magnetotactic bacteria. *Clinical Cancer Research*, 15(16):5170–5177, August 2009.

[103] E. Alphandéry, S. Faure, O. Seksek, F. Guyot, and I. Chebbi. Chains of magnetosomes extracted from AMB-1 magnetotactic bacteria for application in alternative magnetic field cancer therapy. *ACS Nano*, 5(8):6279–6296, August 2011.

[104] R.B. Frankel. Magnetic guidance of organisms. *Annual Review of Biophysics and Bioengineering*, 13:85–103, January 1984.

[105] J. Baumgartner, L. Bertinetti, M. Widdrat, A.M. Hirt, and D. Faivre. Formation of magnetite nanoparticles at low temperature: from superparamagnetic to stable single domain particles. *PloS ONE*, 8(3), January 2013.

[106] G. Muscas, G. Concas, C Cannas, A. Musinu, A. Ardu, F. Orrù, D. Fiorani, S. Laureti, D. Rinaldi, G. Piccaluga, and D. Peddis. Magnetic Properties of Small Magnetite Nanocrystals. *The Journal of Physical Chemistry C*, 117(44):23378–23384, November 2013.

[107] H. Suzuki, T. Tanaka, T. Sasaki, N. Nakamura, T. Matsunaga, and S. Mashiko. High-Resolution Magnetic Force Microscope Images of a Magnetic Particle Chain Extracted from Magnetic Bacteria AMB-1. *Japanese Journal of Applied Physics*, 37(11 Part A):1343–1345, November 1998.

[108] C.E. Diebel, R. Proksch, C.R. Green, P. Neilson, and M.M. Walker. Magnetite defines a vertebrate magnetoreceptor. *Nature*, 406(6793):299–302, July 2000.

[109] E. Alphandéry, A.T. Ngo, C. Lefèvre, I. Lisiecki, L.F. Wu, and M.P. Pileni. Difference between the Magnetic Properties of the Magnetotactic Bacteria and Those of the Extracted Magnetosomes: Influence of the Distance between the Chains of Magnetosomes. *The Journal of Physical Chemistry C*, 112(32):12304–12309, August 2008.

[110] K. Erglis, Q. Wen, V. Ose, A. Zeltins, A. Sharipo, P.A. Janmey, and A. C*f*ìbers. Dynamics of magnetotactic bacteria in a rotating magnetic field. *Biophysical Journal*, 93(4):1402–1412, August 2007.

[111] A. Demortière, P. Panissod, B.P. Pichon, G. Pourroy, D. Guillon, B. Donnio, and S. Bégin-Colin. Size-dependent properties of magnetic iron oxide nanocrystals. *Nanoscale*, 3(1):225–232, January 2011.

[112] A. Witt, K. Fabian, and U. Bleil. Three-dimensional micromagnetic calculations for naturally shaped magnetite: Octahedra and magnetosomes. *Earth and Planetary Science Letters*, 233(3-4):311–324, May 2005.

[113] H.P. Johnson, W. Lowrie, and D.V. Kent. Stability of Anhysteretic Remanent Magnetization in Fine and Coarse Magnetite and Maghemite Particles. *Geophysical Journal International*, 41(1):1–10, April 1975.

[114] U. Gysin, S. Rast, M. Kisiel, C. Werle, and E. Meyer. Low temperature ultrahigh vacuum noncontact atomic force microscope in the pendulum geometry. *The Review of Scientific Instruments*, 82(2), February 2011.

[115] D.-W. Lee, J.-H. Kang, U. Gysin, S. Rast, E. Meyer, M. Despont, and C. Gerber. Fabrication and evaluation of single-crystal silicon cantilevers with ultra-low spring constants. *Journal of Micromechanics and Microengineering*, 15(11):2179–2183, November 2005.

[116] B.N.J. Persson, O. Albohr, U. Tartaglino, A.I. Volokitin, and E. Tosatti. On the nature of surface roughness with application to

contact mechanics, sealing, rubber friction and adhesion. *Journal of Physics: Condensed Matter*, 17(1):1–62, January 2005.

[117] E.R. Beach, G.W. Tormoen, J. Drelich, and R. Han. Pull-off force measurements between rough surfaces by atomic force microscopy. *Journal of Colloid and Interface Science*, 247(1):84–99, March 2002.

[118] M. Götzinger and W. Peukert. Particle Adhesion Force Distributions on Rough Surfaces. *Langmuir*, 20(13):5298–5303, June 2004.

[119] M.H. Korayem and M. Zakeri. Dynamic modeling of manipulation of micro/nanoparticles on rough surfaces. *Applied Surface Science*, 257(15):6503–6513, May 2011.

[120] P. Klapetek, M. Valtr, D. Nečas, O. Salyk, and P. Dzik. Atomic force microscopy analysis of nanoparticles in non-ideal conditions. *Nanoscale Research Letters*, 6(1):514, January 2011.

[121] M. Wasem, J. Köser, S. Hess, E. Gnecco, and E. Meyer. Exploring the retention properties of CaF2 nanoparticles as possible additives for dental care application with tapping-mode atomic force microscope in liquid. *Beilstein Journal of Nanotechnology*, 5:36–43, January 2014.

[122] M. Meincken, D.L. Holroyd, and M. Rautenbach. Atomic force microscopy study of the effect of antimicrobial peptides on the cell envelope of Escherichia coli. *Antimicrobial Agents and Chemotherapy*, 49(10):4085–4092, October 2005.

[123] R.C. Anderson, R.G. Haverkamp, and P.-L. Yu. Investigation of morphological changes to Staphylococcus aureus induced by ovine-derived antimicrobial peptides using TEM and AFM. *FEMS Microbiology Letters*, 240(1):105–110, November 2004.

[124] N.A. Amro, L.P. Kotra, K. Wadu-Mesthrige, A. Bulychev, S. Mobashery, and G.-Y. Liu. High-Resolution Atomic Force Microscopy Studies of the Escherichia coli Outer Membrane: Structural Basis for Permeability. *Langmuir*, 16(6):2789–2796, March 2000.

[125] C.S. Alves, M.N. Melo, H.G. Franquelim, R. Ferre, M. Planas, L. Feliu, E. Bardají, W. Kowalczyk, D. Andreu, N.C. Santos, M. Fernandes, and M. Castanho. Escherichia coli cell surface perturbation and disruption induced by antimicrobial peptides BP100 and pepR. *The Journal of Biological Chemistry*, 285(36):27536–27544, September 2010.

[126] K. Schröter, A. Petzold, T. Henze, and T. Thurn-Albrecht. Quantitative Analysis of Scanning Force Microscopy Data Using Harmonic Models. *Macromolecules*, 42(4):1114–1124, February 2009.

[127] L. Wang. The role of damping in phase imaging in tapping mode atomic force microscopy. *Surface Science*, 429(1-3):178–185, June 1999.

[128] S. Spring, R. Amann, W. Ludwig, K.-H. Schleifer, H. Van Gemerden, and N. Petersen. Dominating Role of an Unusual Magnetotactic Bacterium in the Microaerobic Zone of a Freshwater Sediment. *Applied and Environmental Microbiology*, 59(8):2397–2403, 1993.

[129] K.T. Silva, F. Abreu, C.N. Keim, M. Farina, and U. Lins. Ultrastructure and cytochemistry of lipid granules in the many-celled magnetotactic prokaryote, 'Candidatus Magnetoglobus multicellularis'. *Micron*, 39(8):1387–1392, December 2008.

[130] D.P. Weber, D. Rüffer, A. Buchter, F. Xue, E. Russo-Averchi, R. Huber, P. Berberich, J. Arbiol, A. Fontcuberta I Morral, D. Grundler, and M. Poggio. Cantilever magnetometry of individual Ni nanotubes. *Nano Letters*, 12(12):6139–6144, December 2012.

[131] F. Luis, J. Torres, L. García, J. Bartolomé, J. Stankiewicz, F. Petroff, F. Fettar, J.-L. Maurice, and A. Vaurès. Enhancement of the magnetic anisotropy of nanometer-sized Co clusters: Influence of the surface and of interparticle interactions. *Physical Review B*, 65(9):094409, February 2002.

[132] E. Alphandéry, Y. Ding, A.T. Ngo, Z.L. Wang, L.F. Wu, and M.P. Pileni. Assemblies of aligned magnetotactic bacteria and extracted magnetosomes: what is the main factor responsible for the magnetic anisotropy? *ACS Nano*, 3(6):1539–1547, June 2009.

[133] D. Le Sage, K. Arai, D.R. Glenn, S.J. DeVience, L.M. Pham, L. Rahn-Lee, M.D. Lukin, A. Yacoby, A. Komeili, and R.L. Walsworth. Optical magnetic imaging of living cells. *Nature*, 496(7446):486–489, April 2013.

[134] R. Nadkarni, S. Barkley, and C. Fradin. A comparison of methods to measure the magnetic moment of magnetotactic bacteria through analysis of their trajectories in external magnetic fields. *PloS ONE*, 8(12), January 2013.

[135] M.M. Walker, T.P. Quinn, J.L. Kirschvink, and C. Groot. Production of single-domain magnetite throughout life by sockeye salmon,

Oncorhynchus nerka. *The Journal of Experimental Biology*, 140:51–63, November 1988.

[136] M.M. Walker. Learned magnetic field discrimination in yellowfin tuna,Thunnus albacares. *Journal of Comparative Physiology A*, 155(5):673–679, 1984.

[137] P. M. Davis and M. E. Evans. Interacting single-domain properties of magnetite intergrowths. *Journal of Geophysical Research*, 81(5):989–994, February 1976.

[138] A. Buchter, J. Nagel, D. Rüffer, F. Xue, D.P. Weber, O.F. Kieler, T. Weimann, J. Kohlmann, A.B. Zorin, E. Russo-Averchi, R. Huber, P. Berberich, A. Fontcuberta I Morral, M. Kemmler, R. Kleiner, D. Koelle, D. Grundler, and M. Poggio. Reversal Mechanism of an Individual Ni Nanotube Simultaneously Studied by Torque and SQUID Magnetometry. *Physical Review Letters*, 111(6), August 2013.

List of Symbols and Abbreviations

Symbols

F_N: Normal force
k_N: Normal spring constant
ω_0: Angular resonance frequency
ω: Angular driving frequency
Q: Quality factor
F_{ts}: Tip-sample interaction force
F_0: Excitation force of the actuator
A_{exc}: Excitation amplitude of the actuator
R: Radius of the tip
b: Spacing between consecutive scan lines in slow scan direction
α: Collision angle between tip and particle
A_0: Oscillation amplitude; $f{=}f^{1^{st}}$
A_{osc}: Free oscillation amplitude
A_{sp}: Set point amplitude
η: Viscous damping
P_{in}: Input power to drive oscillation
P_0: Dissipated power of the cantilever body
P_{tip}: Dissipated power by tip-sample interaction
f_0: Free resonance frequency
Δf: Frequency shift
δf: Thermal frequency noise
φ: Phase shift
τ: Cantilever torque
k_B: Boltzmann constant
T: Temperature
H_{ext}: External applied magnetic field
H_{int}: Internal magnetic field
M: Magnetization
$\hat{N}$: Demagnetization tensor
L: Effective length of the cantilever
$\tilde{L}$: Reduced length of the cantilever
w: Thickness of the cantilever
V: Volume
H_c: Coercive field
m: Magnetic moment
K_{eff}: Effective anisotropy constant
K_1: First order magnetocrystalline anisotropy constant

Elements and materials

Ca: Calcium
F: Fluorine
Si: Silicon
O: Oxygen
Fe: Iron

Methods

AFM: Atomic Force Microscopy
SPM: Scanning Probe Microscopy
KPFM: Kelvin Probe Force Microscopy
SEM: Scanning Electron Microscopy
STM: Scanning Tunneling Microscopy
DCM: Dynamic Cantilever Magnetometry

Units

°: Degrees
°C: Degrees Celcius
eV: Electron volts
Hz: Hertz
T: Tesla
K: Kelvin
N: Newtons
g: Grams
m: Meters
min: Minutes
rpm: Revolutions per minutes

Acknowledgements

First of all, I would like to greatly thank Professor Ernst Meyer for giving me the opportunity to make this thesis in his group. Beside creating a very enjoyable and relaxing atmosphere in the group, he was also always present when I needed scientific advise. Next I would like to thank Thilo Glatzel, he was always the person to ask when any kind of problem occurred, either in a scientific, technical or administrative point of view. Without his dedication to the group, the group would not be as nice as it is. A special thank also goes to Marcin Kisiel with whom I worked on two projects together. He proof-read the manuscript. His humble personality and extraordinary knowledge in physics and technical issues were fundamental for me to finish this thesis. I would also like to thank Joachim Köser and Monica Schönenberger for the fruitful joint work. A special thank also goes to Gregor Fessler, Sascha Koch and Markus Langer, my former office partners, for the scientifc discussions and specially for the personal experiences which I really do no want to miss. Many thanks also to Urs Gysin to read the manuscript and for the interesting discussion and to Roland Steiner which was indispensable to create the nice atmosphere in the office although all in the office had to answer a pile of phone calls addressed to him as he was often not in the office. A special thank also to team France, Remy Pawlak, Laurent Marot and Antoine Hinaut, for the friendly and warm atmosphere they created in the group. Thanks also to Gino Günzburger, Mathias Schulzendorf, Tobias Meier, Lucas Moser (the coffee master), Elcin Külah, Sara Freund and Alexander Bubendorf and all other persons from the team.
Last but not least, surely the most important thank goes to my family and my lovely girlfriend, which supported me all the years financially but way more important emotionally when my motivation droped or I was stuck in the work. To my family I owe everything I have in my life.

List of Publications and Communications

Peer-reviewed Journal Publications

- **M. Wasem**, J. Köser, S. Hess, E. Gnecco and E. Meyer. Exploring the retention properties of CaF_2 nanoparticles as possible additives for dental care application with tapping-mode atomic force microscope in liquid. *Beilstein Journal of Nanotechnology*, Volume:5, Page: 36-43, 2014.

- B. N. Persson, A. Kovalev, **M. Wasem**, E. Gnecco, S. N. Gorb. Surface roughness of peeled adhesive tape: A mystery? *Europhysics Letters*, Volume: 92, Page: 46001, 2010.

- J. Zhao, **M. Wasem**, C. R. Bradbury, D. J. Fermin. Charge Transfer across Self-Assembled Nanoscale Metal-Insulator-Metal Heterostructures *Journal of Physical Chemistry C*, Volume: 112, Page: 7284-7289, 2008.

Scientific Communications

- Nanomanipulation Workshop, 25-27 April 2012, Madrid, Spain.

- Swiss Nanoconvention, 23-24 May 2013, Basel, Switzerland.

- NextNanoStars, 21 March 2013, Basel, Switzerland.

- KIT Workshop, 4-5 March 2013, Karlsruhe, Germany.

- KIT Workshop, 24-25 February 2014, Karlsruhe, Germany.

- Nanomanipulation Workshop, 12-14 June 2013, Krakow, Poland.

- Nanomanipulation Workshop, 18-20 June 2014, Mulhouse, France.